

Engineered ionic polymer metal composites (eIPMCs) under dynamic compression loading conditions: theory and experiments

Omid Fakharian¹ , William S Nagel² , Kam K Leang³  and Matteo Aureli^{1,*} 

¹ Department of Mechanical Engineering, University of Nevada, Reno 1664 N Virginia St., Reno, NV 89557-0312, United States of America

² Robotics Engineering Department, Widener University, One University Place, Chester, PA 19013, United States of America

³ Department of Mechanical Engineering and Robotics Center, University of Utah 1495 E. 100 S., Salt Lake City, UT 84112, United States of America

E-mail: maureli@unr.edu

Received 7 September 2024, revised 13 December 2024

Accepted for publication 15 January 2025

Published 30 January 2025



CrossMark

Abstract

Engineered Ionic Polymer Metal Composites (eIPMCs) represent the next generation of IPMCs, soft electro-chemo-mechanically coupled smart materials used as actuators and sensors. Recent studies indicate that eIPMC sensors, featuring unique microstructures at the interface between the ionic polymer membrane and the electrode, exhibit enhanced electrochemical behavior and sensitivity under compression, as compared to traditional IPMCs. However, a complete and experimentally-validated model of how eIPMCs behave under dynamic compression loads is currently missing. In this paper, we develop an analytical model for eIPMC sensors, elucidating the role of the engineered interface, modeled as a separate material layer with unique mechanical and electrochemical properties. Theoretical predictions focus on the mechanical-to-electrochemical transduction response under dynamic compressive loads. Experimental verification is conducted on conventional IPMC and novel eIPMC samples fabricated using the polymer abrading technique. Electrochemical impedance spectroscopy is performed to study the effect of the engineered interface on the electrochemical properties. Open-circuit (OC) voltage and short-circuit (SC) current are measured under external compressive loads in different loading scenarios to demonstrate sensing performance. Results show good qualitative agreement between experimental trends and model predictions. Experiments over the frequency range 1–18 Hz demonstrate an increase of 220%–290% in open-circuit voltage and 17%–166% in SC current sensitivity for eIPMCs over IPMCs.

Keywords: Ionic polymer metal composites, Soft actuator and sensor, Physics-based model, Electrochemical impedance spectroscopy

1. Introduction

There is a critical demand for soft sensors in different applications across various fields such as soft robotics [1],

bioengineering [2], rehabilitation [3], medical devices [4], and human-machine integrated systems [5]. Despite recent advances demonstrated by several classes of widespread sensors such as resistive [6], capacitive [7], piezoelectric [8], and optical fiber [9], existing technologies have disadvantages such as high actuation pressure, non-linearity (due to

* Author to whom any correspondence should be addressed.

output inversely proportional to the gap between the parallel electrodes), low flexibility, and post-processing difficulty, respectively. Hence, there is a need for developing new types of soft sensors with improved capabilities.

Ionic polymer-metal composites (IPMCs) are a class of electroactive smart materials fabricated from a thin electrically charged polymer membrane, such as Nafion, plated with noble metal electrodes, such as platinum, then neutralized with a charged solvent [10]. Inherent properties of IPMCs, such as their flexibility [11], self-sensing capacity [12], and operation in both air and water environments [13], make them an ideal candidate in various engineering applications [3, 4]. IPMCs have the ability to operate as both sensors and actuators [14, 15]; however, most of the research work on IPMCs has focused on their actuation mode. Among the studies of the sensor mode, the majority have focused on bending mode sensing [16–18], with fewer studies concentrating on the feasibility of IPMCs sensors as force and displacement sensors [19–22] or energy harvesting systems [23–27]. The common challenges of low sensitivity, poor property control, and non-versatile operation of IPMCs sensors, have limited their use in applications outside of the typical bending-mode configuration [28], and only a few studies investigate IPMC sensors under compression [29–34] and shear sensing [35, 36]. In particular, IPMCs show high variability in their electrochemical properties, including capacitance [37].

To understand the fundamental behavior of IPMCs under compression loading conditions and overcome some of the fundamental limitations in terms of sensing, our group has developed *engineered* IPMCs (eIPMCs) [28, 38]. In the eIPMCs, one polymer-electrode interface in the material is purposefully modified to enhance inhomogeneous (and, possibly, anisotropic) strain fields upon compression. In [38], the interface modification is produced via a novel fabrication method called the ‘polymer abrading technique’ (PAT). Unlike additive manufacturing approaches [28], PAT is advantageous due to its repeatability, simplicity, and cost-effectiveness, as it does not require specialized 3D printing equipment. In our recent works [38, 39], we focused on the performances of the eIPMC sensor fabricated using PAT under static and quasi-static compression and bending loading conditions. In [28], we developed a new eIPMC model which captures the process-structure relationships and illustrates the enhanced sensitivity of eIPMC sensors. In [39], we presented an updated, simplified minimal mechano-chemo-electrical model for the eIPMC sample under both compression and bending. This model describes mechanical inhomogeneities in a more intuitive way by assuming a separate composite layer (CL) for the engineered interface. Crucially, while the CL has different mechanical properties than the bulk polymer, the electromechanical properties are assumed to be the same. While correctly identifying the mechanism for mechano-chemoelectrical transduction, this model cannot capture important features of the sensor dynamic response that are observed experimentally.

In this paper, we aim to address three specific knowledge gaps identified in previous work. First, we introduce a novel analytical model that correctly includes both the mechanical and electrochemical properties of the CL in eIPMC. The model

is attacked analytically, and allows us to understand the physics of the sensor response under both static and dynamic compressive loads. Finally, the model enables a complete characterization of sensing modes beyond the open-circuit (OC) voltage sensing. Our novel model is verified experimentally, with results showing agreement between our analytical predictions and experimental findings.

The key contributions and novelties of this article include: (1) a novel physics-based model that explores the sensing behavior of eIPMCs under dynamic compressive loads. The engineered interface of the eIPMC is modeled as a separate layer with unique mechanical and electrochemical properties. We note that an asymmetric CL with unique mechanical and electrochemical properties, which is a natural description of an engineered interface, was never considered in the literature; (2) experimental measurement of OC voltage performance of eIPMCs under dynamic compressive loads, demonstrating the agreement between experimental observations and theoretical results; and (3) an evaluation of the short-circuit (SC) current performance of eIPMCs under dynamic compressive loads, and its favorable comparison with our modeling results. Note that the SC current response, while predicted theoretically, was never experimentally studied in the context of eIPMCs.

The remainder of the paper is organized as follows. Section 2 presents the new physics-based model of the mechano-chemo-electrical behavior of the eIPMC under dynamic external compressive loads. Section 3 reports on the fabrication and electrochemical characterization of our novel eIPMC sensors. Section 4 details the OC voltage and SC current sensing performance measurement, where the response to single sine, step, and chirp load is evaluated and interpreted, in light of the modeling results. Section 5 presents a discussion of the findings of this work. Concluding remarks are presented in section 6.

2. Modeling and governing equations

2.1. Problem statement and nomenclature

This section focuses on the chemoelectromechanical transduction via a one-dimensional through-the-thickness (TTT) problem described by the spatial coordinate, denoted here as x . The schematic representation and nomenclature of the problem are depicted in figure 1, where figure 1(a) shows a TTT schematics of the eIPMC with idealized engineered micro-features and figure 1(b) presents a model based on homogenization of the engineered interface, see also [40]. In this model, the engineered interface between the polymer and the metal regions is modeled with a CL. Because of the homogenization approach, we will consistently neglect the specific description of electrode surface roughness [37, 41]. As sketched in figure 1(b), the thickness of the bulk region is assumed to be $2h$, the CL is between $-d \leq x \leq 0$, the grounded (fixed) electrode is at $x = -d$. The grounded electrode is at zero electric potential, that is, $V = 0$. A time-varying compressive load $p(t)$ is applied to the upper (movable) electrode at $x = 2h$, and the output voltage V is measured from this electrode.

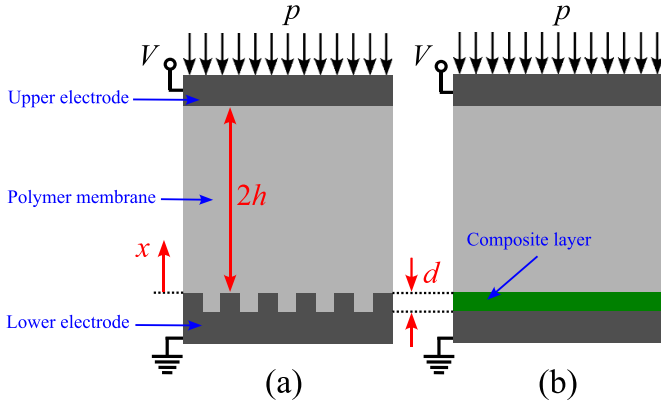


Figure 1. Schematic representation (not to scale) and nomenclature of eIPMC, with (a) detail of the idealized engineered interface region, and (b) the homogenization as CL region. Here, V is the electric potential at the movable electrode, p is the exerted pressure, h is the semi-thickness of the bulk polymer membrane, d is the thickness of the CL, and x is the through-the-thickness coordinate.

Throughout this work, we focus on the relatively low-frequency behavior of the eIPMC sensor. In particular, we systematically neglect dynamic effects on the mechanics time scale (which is assumed to respond much slower than the chemo-electrical time scale). Furthermore, we neglect high frequency behavior in the chemo-electrical response, similar to previous approaches discussed in the literature, see for example [28, 39].

2.2. Simplified mechanical model

A simplified model for the mechanical behavior of eIPMCs under compression was proposed in [28] and further refined in [39]. Within this approach, the composite was modeled as a sandwich material comprised of two rigid layers (movable and fixed electrodes) and two isotropic and homogeneous layers (bulk polymer and interfacial layers) with different mechanical properties, for example see also figure 1(b). In particular, the Young's modulus of the CL is expressed via the 'inverse rule of mixtures', under the assumption of uniform stress in the CL. We indicate the Young's modulus of the polymer, metal, and CL by E_p , E_m , and E_{cl} , respectively. Thus, $E_{cl} = [\phi/E_p + (1 - \phi)/E_m]^{-1}$, where ϕ is the volume fraction of the polymer (volume of polymer per unit volume of the interface) and can be potentially estimated by the interfacial topography, for example see [39]. Specifically, for the idealized interface schematically depicted in figure 1(a), we would have $\phi = 0.5$. Because $E_m \gg E_p$, the estimate of E_{cl} can be approximated with $E_{cl} \approx E_p/\phi$. As explained later, however, the explicit values of ϕ and d which would be difficult to measure experimentally are not needed in the final version of the model. At any rate, it is possible to indirectly estimate these quantities from electrochemical tests as discussed in [39].

According to the previous development, under the application of an external compressive load, a uniaxial state of stress develops in the TTT direction. Assuming plane strain conditions and uniform stresses at each x location, the strain in

the TTT direction in the bulk polymer region (superscript p) is $\epsilon_x^p = -p(t)/E_p$, whereas the strain in the CL region (superscript cl) is $\epsilon_x^{cl} = -p(t)/E_{cl}$. Because of the homogenization approach, we assume null strain in the in-plane direction $\epsilon_y = 0$ throughout the material and we neglect stress concentrations. This hypothesis is a simplification of the complicated nature of the TTT stress and strain profiles as discussed in [28]. In response to compression, the material undergoes volumetric changes described by the dilatation (trace of the strain tensor) that, in the bulk polymer and in the CL regions, can be expressed as $\Delta = \epsilon_x^p = -p(t)/E_p$, and $\Delta_{cl} = \epsilon_x^{cl} = -p(t)/E_{cl} \approx -\phi p(t)/E_p$, respectively. This implies that $\Delta_{cl} \approx \phi \Delta$. Importantly, the mechanical asymmetry between the properties of the bulk polymer and the CL result in inhomogeneous strain in the TTT direction which is responsible for mechanical to electrochemical transduction. Results of this minimal mechanical modeling approach will be used in the next section to couple the electrochemical description of eIPMCs to the external mechanical excitation.

2.3. Linear chemoelectromechanical sensing model

Herein, we present the model for mechanical to electrochemical transduction by postulating linear response for the eIPMC as a compression sensor, assuming small deformations, electric potentials, and deviations of the counterion concentration from the concentration at rest. Compared to our previous work [39] where the bulk and the CL regions differed only by their mechanical properties, here we extend the analysis to also include electrochemical property differences between these regions. Throughout this work, the polymer and the CL are assumed to be electrochemically homogeneous and isotropic, and it is assumed that the eIPMC electrodes are perfectly conductive.

The nonlinear governing equations for the mechano-chemo-electrical sensing behavior of IPMC have been previously formulated in [17, 30, 42]. The linearized version of the Equations for the bulk region are provided by [39]. The linearized equations for the eIPMC bulk region are

$$-\varepsilon \frac{\partial^2 \psi(x,t)}{\partial x^2} = \mathcal{F} \{c(x,t) - c_0 [1 - \Delta(x,t)]\}, \quad (1a)$$

$$\frac{\partial}{\partial t} [c(x,t) + c_0 \Delta(x,t)] = \mathcal{D} \left[\frac{\partial^2 c(x,t)}{\partial x^2} + \frac{\mathcal{F} c_0}{\mathcal{RT}} \frac{\partial^2 \psi(x,t)}{\partial x^2} \right]. \quad (1b)$$

Equation (1a) defines Poisson's equation, establishing the correlation between the electric potential ψ and the free charge in the eIPMC based on Gauss' law. Here, \mathcal{F} represents Faraday's constant, c is the concentration of mobile counterions, c_0 is the concentration of fixed ions, and ε is the bulk polymer permittivity, assumed to be constant. We emphasize that the concentrations of mobile counterions and fixed ions are computed with respect to the deformed volume of the eIPMC. Other approaches are also possible, see for example [16]. Equation (1b) represents the linearized generalized Nernst-Planck equation, ensuring the conservation

of charge in the eIPMC. Here, \mathcal{D} is the counterion diffusivity in the bulk polymer, \mathcal{R} is the universal gas constant, and \mathcal{T} denotes the IPMC temperature. The right-hand side of equation (1b) can be interpreted as the negative divergence of the linearized ion flux J , expressed as $J(x, t) = -\mathcal{D}[\partial c(x, t)/\partial x + (\mathcal{F}c_0)/(\mathcal{R}\mathcal{T})\partial\psi(x, t)/\partial x]$. Similarly, the left-hand side of equation (1a) can be interpreted as the divergence of the electric displacement $D(x, t) = -\varepsilon\partial\psi(x, t)/\partial x$.

Using similar linear assumptions as in the bulk region, the governing equations for the sensing behavior in the CL are expressed as

$$-\varepsilon_{cl}\frac{\partial^2\psi_{cl}(x, t)}{\partial x^2} = \mathcal{F}\{c_{cl}(x, t) - c_0\phi[1 - \Delta_{cl}(x, t)]\}, \quad (2a)$$

$$\begin{aligned} \frac{\partial}{\partial t}[c_{cl}(x, t) + c_0\phi\Delta_{cl}(x, t)] \\ = \mathcal{D}_{cl}\left[\frac{\partial^2 c_{cl}(x, t)}{\partial x^2} + \frac{\mathcal{F}c_0\phi}{\mathcal{R}\mathcal{T}}\frac{\partial^2\psi_{cl}(x, t)}{\partial x^2}\right], \end{aligned} \quad (2b)$$

where the subscript cl indicates quantities pertaining to the CL. It should be noticed that in the CL the concentration of fixed ions is given by $c_0\phi$ due to the presence of the metal phase, see also [40]. Additionally, the ion flux and the electric displacement in the CL are $J_{cl}(x, t) = -\mathcal{D}_{cl}[\partial c_{cl}(x, t)/\partial x + (\mathcal{F}c_0\phi)/(\mathcal{R}\mathcal{T})\partial\psi_{cl}(x, t)/\partial x]$ and $D_{cl}(x, t) = -\varepsilon_{cl}\partial\psi_{cl}(x, t)/\partial x$, respectively.

The governing equations above must be supplemented with initial, boundary, and continuity conditions. For ease of presentation, these will be discussed below in their nondimensional form.

2.4. Nondimensionalization

It is convenient to nondimensionalize the governing equations for both the bulk region and CL. For the bulk region, we introduce the following nondimensional variables, indicated by superimposed tilde: nondimensional length $\tilde{x} = x/h$ and time $\tilde{t} = t/t_0$, pressure $\tilde{p}(\tilde{t}) = p(t_0\tilde{t})/E_p$, voltage $\tilde{\psi}(\tilde{x}, \tilde{t}) = \psi(h\tilde{x}, t_0\tilde{t})/V_{th}$, net counterion concentration $\tilde{\chi}(\tilde{x}, \tilde{t}) = (c(h\tilde{x}, t_0\tilde{t}) - c_0)/c_0$, and ion flux $\tilde{J}(\tilde{x}, \tilde{t}) = -(\mathcal{D}c_0/h)(\partial[\tilde{\chi}(\tilde{x}, \tilde{t}) + \tilde{\psi}(\tilde{x}, \tilde{t})]/\partial\tilde{x})$. The parameters t_0 is a characteristic time that will be defined later. Similarly, $V_{th} = \mathcal{R}\mathcal{T}/\mathcal{F}$ is a characteristic voltage known as the thermal voltage, approximately equal to 25 mV at room temperature. Thus, the nondimensional form of equations (1a) and (1b) is expressed as

$$-\delta^2\frac{\partial^2\tilde{\psi}(\tilde{x}, \tilde{t})}{\partial\tilde{x}^2} = \tilde{\chi}(\tilde{x}, \tilde{t}) - \tilde{p}(\tilde{t}), \quad (3a)$$

$$\frac{\partial}{\partial\tilde{t}}[\tilde{\chi}(\tilde{x}, \tilde{t}) - \tilde{p}(\tilde{t})] = \delta\left[\frac{\partial^2\tilde{\chi}(\tilde{x}, \tilde{t})}{\partial\tilde{x}^2} + \frac{\partial^2\tilde{\psi}(\tilde{x}, \tilde{t})}{\partial\tilde{x}^2}\right]. \quad (3b)$$

Here, the parameter $\delta = \lambda_D/h$ is the ratio between the Debye screening length $\lambda_D = \sqrt{(\varepsilon\mathcal{R}\mathcal{T})/(\mathcal{F}^2c_0)}$ and the polymer semithickness h . The characteristic time $t_0 = (\lambda_D h)/\mathcal{D}$ is chosen as the diffusion timescale within the charge boundary

layers. Selecting this timescale allows for a convenient separation of the evolution of mechanical and electrochemical phenomena, see [41].

The CL is significantly thinner than the bulk region, necessitating magnification. Simultaneously conducting magnification and nondimensionalization, we introduce a new spatial coordinate x_{cl} for the CL, with the nondimensional form $\tilde{x}_{cl} = -x/(h\sqrt{\delta})$. Nondimensional variables in the CL are: $\tilde{\psi}_{cl}(\tilde{x}_{cl}, \tilde{t}) = \psi_{cl}(h\tilde{x}_{cl}, t_0\tilde{t})/V_{th}$, $\tilde{\chi}_{cl}(\tilde{x}_{cl}, \tilde{t}) = (c_{cl}(h\tilde{x}_{cl}, t_0\tilde{t}) - c_0\phi)/c_0\phi$, $\tilde{J}_{cl}(\tilde{x}_{cl}, \tilde{t}) = (\mathcal{D}_{cl}c_0\phi/h\sqrt{\delta})(\partial[\tilde{\chi}_{cl}(\tilde{x}_{cl}, \tilde{t}) + \tilde{\psi}_{cl}(\tilde{x}_{cl}, \tilde{t})]/\partial\tilde{x}_{cl})$, and $\tilde{\Delta}_{cl}(\tilde{t}) = -a\tilde{p}(\tilde{t})$, where $a = [\phi + (1 - \phi)E_p/E_m]$ encodes information on the mechanical asymmetry of the CL and the bulk polymer. The nondimensional form of equations (2a) and (2b) read

$$-\varepsilon^*\frac{\partial^2\tilde{\psi}_{cl}(\tilde{x}_{cl}, \tilde{t})}{\partial\tilde{x}_{cl}^2} = \tilde{\chi}_{cl}(\tilde{x}_{cl}, \tilde{t}) - a\tilde{p}(\tilde{t}), \quad (4a)$$

$$\begin{aligned} \frac{\partial}{\partial\tilde{t}}[\tilde{\chi}_{cl}(\tilde{x}_{cl}, \tilde{t}) - a\tilde{p}(\tilde{t})] \\ = \mathcal{D}^*\delta\left[\frac{\partial^2\tilde{\chi}_{cl}(\tilde{x}_{cl}, \tilde{t})}{\partial\tilde{x}_{cl}^2} + \frac{\partial^2\tilde{\psi}_{cl}(\tilde{x}_{cl}, \tilde{t})}{\partial\tilde{x}_{cl}^2}\right]. \end{aligned} \quad (4b)$$

Here, the nondimensional permittivity and diffusivity constants are defined as $\varepsilon^* = \varepsilon_{cl}\delta/(\varepsilon\phi)$ and $\mathcal{D}^* = \mathcal{D}_{cl}/(\mathcal{D}\delta)$. Importantly, because $\varepsilon_{cl} \gg \varepsilon$ and $\mathcal{D}_{cl} \ll \mathcal{D}$, see [40], the parameters ε^* and \mathcal{D}^* are assumed to be of order $\mathcal{O}(1)$, see also [32].

The governing differential equations are supplemented by initial, boundary, and continuity conditions. In particular, we assume that, initially, the polymer and CL are unstressed and electrically neutral. Thus, we let

$$\tilde{p}(\tilde{t} = 0) = 0, \quad (5a)$$

$$\tilde{\psi}(\tilde{x}, \tilde{t} = 0) = 0, \quad (5b)$$

$$\tilde{\psi}_{cl}(\tilde{x}_{cl}, \tilde{t} = 0) = 0, \quad (5c)$$

$$\tilde{\chi}(\tilde{x}, \tilde{t} = 0) = 0, \quad (5d)$$

$$\tilde{\chi}_{cl}(\tilde{x}_{cl}, \tilde{t} = 0) = 0. \quad (5e)$$

Continuity conditions at the bulk polymer-CL interface involve the continuity of electric potential, ion flux, electric displacement, and counterion concentration. These conditions are expressed as

$$\tilde{\psi}(\tilde{x} = 0, \tilde{t}) = \tilde{\psi}_{cl}(\tilde{x}_{cl} = 0, \tilde{t}), \quad (6a)$$

$$\tilde{J}(\tilde{x} = 0, \tilde{t}) = \tilde{J}_{cl}(\tilde{x}_{cl} = 0, \tilde{t}), \quad (6b)$$

$$\tilde{D}(\tilde{x} = 0, \tilde{t}) = \tilde{D}_{cl}(\tilde{x}_{cl} = 0, \tilde{t}), \quad (6c)$$

$$\tilde{\chi}(\tilde{x} = 0, \tilde{t}) = \tilde{\chi}_{cl}(\tilde{x}_{cl} = 0, \tilde{t}). \quad (6d)$$

Finally, we assume ion blocking conditions (null flux at the electrode interfaces), and imposed voltage at the electrodes. We thus have

$$\tilde{J}(\tilde{x} = 2, \tilde{t}) = 0, \quad (7a)$$

$$\tilde{J}_{cl}(\tilde{x}_{cl} = d^*, \tilde{t}) = 0, \quad (7b)$$

$$\tilde{\psi}(\tilde{x} = 2, \tilde{t}) = \tilde{V}(\tilde{t}), \quad (7c)$$

$$\tilde{\psi}_{cl}(\tilde{x}_{cl} = d^*, \tilde{t}) = 0, \quad (7d)$$

where we defined with $d^* = d/(h\sqrt{\delta})$ the nondimensionalized location of the fixed grounded electrode. Note that the voltage $\tilde{V}(\tilde{t})$ is the sensor voltage output measured at the movable electrode, located at the nondimensional distance $\tilde{x} = 2$.

It is important to observe that, in practical applications, $\lambda_D \approx 10^{-10}$ m, rendering the parameter δ of the order of 10^{-6} , see [43]. Consequently, a small parameter multiplies the highest order derivative terms and equations (3a), (3b), (4a) and (4b) describe a singularly perturbed system, amenable to solution through the matched asymptotic expansions method [44]. It is known that, mathematically, this describes the development of a boundary layer solution, reflected physically in a charge boundary layer distribution, see also [43]. Throughout the remaining derivations, the superscript tilde will be omitted for notational convenience.

2.5. Matched asymptotic expansions

The problem is solved using the matched asymptotic expansions method which is a powerful tool for solving boundary value problems with boundary layer-type behaviors. This subsection outlines the solution procedure of this method, following in part [30, 43]. Figure 2 illustrates the general idea and relevant nomenclature, showing two outer expansions and four inner expansions. In the polymer region, we use one inner expansion at the polymer-top electrode interface, an outer expansion for the bulk region, and another inner expansion at the polymer-CL interface. This solution follows closely the one presented in [28]. Conversely, for the CL, we use one inner expansion at the CL-polymer interface, an outer expansion for the CL, and another inner expansion at the CL-grounded electrode interface. This solution is a novel contribution of this work.

2.5.1. Outer expansion for the polymer region. In the eIPMC polymer region, we consider a regular asymptotic expansion of χ and ψ in terms of the small parameter δ , such that $\chi^{(B)}(x, t) = \chi_0^{(B)}(x, t) + \delta\chi_1^{(B)}(x, t) + \delta^2\chi_2^{(B)}(x, t) + \dots$ and $\psi^{(B)}(x, t) = \psi_0^{(B)}(x, t) + \delta\psi_1^{(B)}(x, t) + \delta^2\psi_2^{(B)}(x, t) + \dots$, where the symbol (B) indicates the outer expansion in the bulk region. Substituting these representations in equations (3a) and (3b), and approximating the outer solution with its leading order term of $\mathcal{O}(\delta^0)$, we obtain

$$\chi^{(B)}(x, t) \approx \chi_0^{(B)}(x, t) = p(t), \quad (8a)$$

$$\psi^{(B)}(x, t) \approx \psi_0^{(B)}(x, t) = -p(t) + A_1^{(B)}(t)x + A_0^{(B)}(t), \quad (8b)$$

where $A_1^{(B)}(t)$ and $A_0^{(B)}(t)$ are unknown integration parameters, functions of time.

2.5.2. Inner expansions in the polymer. In the vicinity of polymer-CL interface at $x = 0$ and the interface between the polymer and the top (movable) electrode at $x = 2$, we magnify the spatial coordinate by introducing the stretched variables $\xi_f = x/\delta$ and $\xi_e = (2 - x)/\delta$, respectively. We perform the change of variables in equations (3a) and (3b) and use a regular asymptotic expansion of χ and ψ in the boundary layer region near the polymer-CL interface in terms of the small parameter δ , such that $\chi^{(F)}(\xi_f, t) = \chi_0^{(F)}(\xi_f, t) + \delta\chi_1^{(F)}(\xi_f, t) + \delta^2\chi_2^{(F)}(\xi_f, t) + \dots$ and $\psi^{(F)}(\xi_f, t) = \psi_0^{(F)}(\xi_f, t) + \delta\psi_1^{(F)}(\xi_f, t) + \delta^2\psi_2^{(F)}(\xi_f, t) + \dots$, where the symbol (F) indicates the inner expansion in the boundary layer at the bottom of the polymer (region (F)). Retaining only the leading order, we obtain

$$-\frac{\partial^2 \psi_0^{(F)}(\xi_f, t)}{\partial \xi_f^2} = \chi_0^{(F)}(\xi_f, t) - p(t), \quad (9a)$$

$$\frac{\partial^2}{\partial \xi_f^2} \left[\chi_0^{(F)}(\xi_f, t) + \psi_0^{(F)}(\xi_f, t) \right] = 0. \quad (9b)$$

Notably, the scaling removes the explicit time derivatives from the leading order of equation (3b), which thus reduces to an ordinary differential equation in the spatial variable. By approximating $\chi^{(F)}(\xi_f, t)$ and $\psi^{(F)}(\xi_f, t)$ with their $\mathcal{O}(\delta^0)$ terms, we obtain

$$\chi^{(F)}(\xi_f, t) \approx \chi_0^{(F)}(\xi_f, t) = p(t) + A_1^{(F)}(t)e^{-\xi_f}, \quad (10a)$$

$$\psi^{(F)}(\xi_f, t) \approx \psi_0^{(F)}(\xi_f, t) = -p(t) - A_1^{(F)}(t)e^{-\xi_f} + A_3^{(F)}(t). \quad (10b)$$

Similarly, for the top part of the polymer (region (E)), we have

$$\chi^{(E)}(\xi_e, t) \approx \chi_0^{(E)}(\xi_e, t) = p(t) + A_1^{(E)}(t)e^{-\xi_e}, \quad (11a)$$

$$\psi^{(E)}(\xi_e, t) \approx \psi_0^{(E)}(\xi_e, t) = -p(t) - A_1^{(E)}(t)e^{-\xi_e} + A_3^{(E)}(t), \quad (11b)$$

where $A_1^{(F)}(t)$, $A_3^{(F)}(t)$, $A_1^{(E)}(t)$, and $A_3^{(E)}(t)$ are unknown integration parameters, functions of time. In the derivation of equations (10a), (10b), (11a), and (11b) we have also used the fact that these solutions must be bounded at $\xi_f \rightarrow \infty$ and $\xi_e \rightarrow \infty$.

2.5.3. Outer expansion for the CL region. In the eIPMC CL, we consider a regular asymptotic expansion of χ and ψ in terms of the small parameter $\sqrt{\delta}$, such that $\chi^{(C)}(x_{cl}, t) = \chi_0^{(C)}(x_{cl}, t) + \sqrt{\delta}\chi_1^{(C)}(x_{cl}, t) + \delta\chi_2^{(C)}(x_{cl}, t) + \dots$ and $\psi^{(C)}(x_{cl}, t) = \psi_0^{(C)}(x_{cl}, t) + \sqrt{\delta}\psi_1^{(C)}(x_{cl}, t) + \delta\psi_2^{(C)}(x_{cl}, t) + \dots$, where the symbol (C) indicates the outer expansion in the CL. Substituting these representations in equations (4a) and (4b) and using the initial condition of equation (5e) and by approximating the outer solution with its leading order term, we obtain

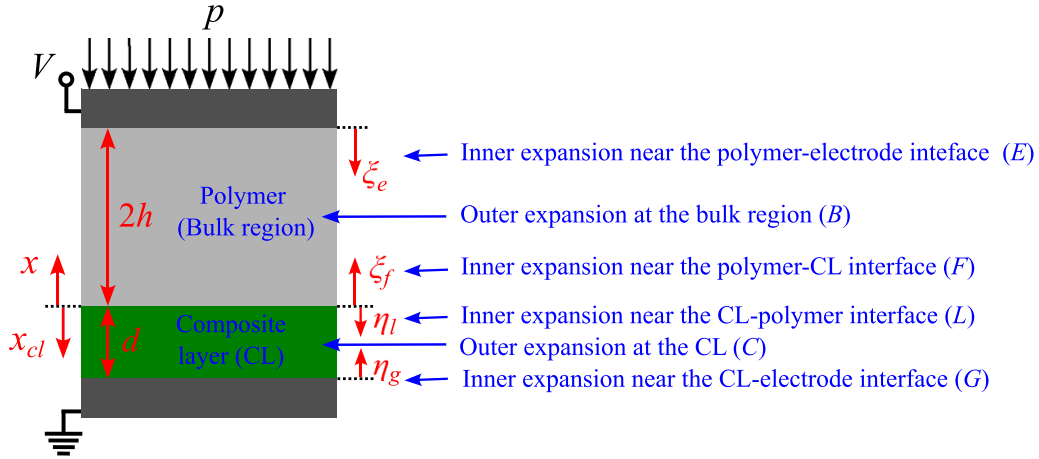


Figure 2. Schematic depiction of matched asymptotic expansions strategy with labels for six expansion zones.

$$\chi^{(C)}(x_{cl}, t) \approx \chi_0^{(C)}(x_{cl}, t) = ap(t), \quad (12a)$$

$$\psi^{(C)}(x_{cl}, t) \approx \psi_0^{(C)}(x_{cl}, t) = C_1^{(C)}(t)x_{cl} + C_0^{(C)}(t), \quad (12b)$$

where $C_1^{(C)}(t)$ and $C_0^{(C)}(t)$ are unknown integration parameters, functions of time.

2.5.4. Inner expansions in the CL. In the vicinity of polymer-CL interface at $x_{cl} = 0$ and CL-electrode interface at $x_{cl} = d^*$, we magnify the spatial coordinate by introducing the stretched variables $\eta_l = x_{cl}/\sqrt{\delta}$ and $\eta_g = (d^* - x_{cl})/\sqrt{\delta}$, respectively. We perform the change of variables in equations (4a) and (4b) and use a regular asymptotic expansion of χ and ψ in the boundary layer region in terms of the small parameter $\sqrt{\delta}$, such that $\chi^{(L)}(\eta_l, t) = \chi_0^{(L)}(\eta_l, t) + \sqrt{\delta}\chi_1^{(L)}(\eta_l, t) + \delta\chi_2^{(L)}(\eta_l, t) + \dots$ and $\psi^{(L)}(\eta_l, t) = \psi_0^{(L)}(\eta_l, t) + \sqrt{\delta}\psi_1^{(L)}(\eta_l, t) + \delta\psi_2^{(L)}(\eta_l, t) + \dots$, where the symbol (L) indicates the inner expansion in the boundary layer at the top of the CL. Thus, at the leading order, equations (4a) and (4b) reduce to

$$\frac{\partial^2 \psi_0^{(L)}(\eta_l, t)}{\partial \eta_l^2} = 0, \quad (13a)$$

$$\frac{\partial}{\partial t} [\chi_0^{(L)}(\eta_l, t) - ap(t)] = \mathcal{D}^* \frac{\partial^2 \chi_0^{(L)}(\eta_l, t)}{\partial \eta_l^2}. \quad (13b)$$

By approximating $\psi^{(L)}(\xi_l, t)$ with its $\mathcal{O}(\delta^0)$ term, we obtain from equation (13a)

$$\psi^{(L)}(\xi_l, t) = \psi_0^{(L)}(\xi_l, t) = C_0^{(L)}(t). \quad (14)$$

Similarly, in the vicinity of CL-electrode interface, the governing equations reduce to

$$\frac{\partial^2 \psi_0^{(G)}(\eta_g, t)}{\partial \eta_g^2} = 0, \quad (15a)$$

$$\frac{\partial}{\partial t} [\chi_0^{(G)}(\eta_g, t) - ap(t)] = \mathcal{D}^* \frac{\partial^2 \chi_0^{(G)}(\eta_g, t)}{\partial \eta_g^2}. \quad (15b)$$

Note that, differently to what observed in the inner expansions in the polymer, the scaling in the CL region does not eliminate the time derivatives in the generalized Nernst-Planck equations. A physical interpretation of the different behavior can be sought in the limited diffusion in the CL, where the ion concentration cannot track the volumetric changes ‘instantaneously’ (at the leading order).

By approximating $\psi^{(G)}$ with its $\mathcal{O}(\delta^0)$ term, we obtain from equation (15a)

$$\psi^{(G)}(\eta_g, t) = \psi_0^{(G)}(\eta_g, t) = C_0^{(G)}(t). \quad (16)$$

In equations (14) and (16), $C_0^{(L)}(t)$ and $C_0^{(G)}(t)$ are unknown integration parameters, functions of time. In addition, in the derivation of these equations, we have also used the fact that the solutions must be bounded at $\eta_l \rightarrow \infty$ and $\eta_g \rightarrow \infty$.

To solve for $\chi_0^{(L)}(\eta_l, t)$ and $\chi_0^{(G)}(\eta_g, t)$, we apply the Laplace transform on equations (13b) and (15b) and indicate transformed variable with a superimposed hat. The transformation reduces the partial differential equations to ordinary differential equations in the independent spatial variable. The solution at the leading order can be easily determined, in the Laplace domain, as $\hat{\chi}^{(L)}(\eta_l, s) \approx \hat{\chi}_0^{(L)}(\eta_l, s) = a\hat{p}(s) + \hat{C}_3^{(L)}(s)e^{-\eta_l\sqrt{s/\mathcal{D}^*}}$ and $\hat{\chi}^{(G)}(\eta_g, s) \approx \hat{\chi}_0^{(G)}(\eta_g, s) = a\hat{p}(s) + \hat{C}_3^{(G)}(s)e^{-\eta_g\sqrt{s/\mathcal{D}^*}}$ with s the complex Laplace (nondimensional) variable. These solutions indicate a diffusion-dominated dynamics for the ion concentration. Similar behaviors were observed in [32], where a solution based on heat kernels was developed for a related problem.

Here, $\hat{C}_3^{(L)}(s)$ and $\hat{C}_3^{(G)}(s)$ are unknown integration functions of time that have been transformed in the Laplace domain. To determine these functions, along with the other unknown functions of time of the previous developments, we first take the Laplace-transform of equations (8a), (8b), (10a), (10b), (11a), (11b), (12a), (12b), (14) and (16). Then, we determine the unknown functions by imposing the matching conditions. In the following, all functions are assumed

to be transformed into the Laplace domain (unless otherwise specified) and the superimposed hat will be dropped for simplicity.

2.5.5. Matching. The inner and outer expansions determined above must be matched in such a way they share a common limit in their overlap regions. The matching conditions consist of the following limit conditions

$$\lim_{x \rightarrow 2} \psi^{(B)}(x, s) = \lim_{\xi_e \rightarrow \infty} \psi^{(E)}(\xi_e, s), \quad (17a)$$

$$\lim_{x \rightarrow 2} \chi^{(B)}(x, s) = \lim_{\xi_e \rightarrow \infty} \chi^{(E)}(\xi_e, s), \quad (17b)$$

$$\lim_{x \rightarrow 0} \psi^{(B)}(x, s) = \lim_{\xi_f \rightarrow \infty} \psi^{(F)}(\xi_f, s), \quad (17c)$$

$$\lim_{x \rightarrow 0} \chi^{(B)}(x, s) = \lim_{\xi_f \rightarrow \infty} \chi^{(F)}(\xi_f, s), \quad (17d)$$

$$\lim_{x_{cl} \rightarrow 0} \psi^{(C)}(x_{cl}, s) = \lim_{\eta_l \rightarrow \infty} \psi^{(L)}(\eta_l, s), \quad (17e)$$

$$\lim_{x_{cl} \rightarrow 0} \chi^{(C)}(x_{cl}, s) = \lim_{\eta_l \rightarrow \infty} \chi^{(L)}(\eta_l, s), \quad (17f)$$

$$\lim_{x_{cl} \rightarrow d^*} \psi^{(C)}(x_{cl}, s) = \lim_{\eta_g \rightarrow \infty} \psi^{(G)}(\eta_g, s), \quad (17g)$$

$$\lim_{x_{cl} \rightarrow d^*} \chi^{(C)}(x_{cl}, s) = \lim_{\eta_g \rightarrow \infty} \chi^{(G)}(\eta_g, s). \quad (17h)$$

Substituting in the proper leading-order solutions, we obtain,

$$2A_1^{(B)}(s) + A_0^{(B)}(s) = A_3^{(E)}(s), \quad (18a)$$

$$A_0^{(B)}(s) = A_3^{(F)}(s), \quad (18b)$$

$$C_0^{(C)}(s) = C_0^{(L)}(s), \quad (18c)$$

$$C_1^{(C)}(s)d^* + C_0^{(C)}(s) = C_0^{(G)}(s). \quad (18d)$$

The next matching condition pertains to enforcing the voltage boundary conditions given by equations (7c) and (7d). Thus,

$$\psi^{(G)}(\eta_g = 0, s) = C_0^{(G)}(s) = 0, \quad (19a)$$

$$\psi^{(E)}(\xi_e = 0, s) = -p(s) - A_1^{(E)}(s) + A_3^{(E)}(s) = V(s). \quad (19b)$$

The electric potential and charge concentration continuity conditions yield

$$p(s) + A_1^{(F)}(s) = ap(s) + C_3^{(L)}, \quad (20a)$$

$$-p(s) - A_1^{(F)}(s) + A_3^{(F)}(s) = C_0^{(L)}(s). \quad (20b)$$

The other matching condition is the continuity of the ion flux at the polymer-CL interface and can be enforced by adapting the procedure in [32, 43]. For this, we temporarily revert to the time domain description. By integrating (3b) from the polymer-CL interface to an arbitrary location in the polymer region we have

$$\begin{aligned} & \frac{\partial}{\partial t} \int_0^x [\chi(x', t) - p(t)] dx' \\ &= \delta \frac{\partial}{\partial x} [\chi(x, t) + \psi(x, t)] \\ & - \delta \frac{\partial}{\partial x} [(\chi(x=0, t) + \psi(x=0, t))]. \end{aligned} \quad (21)$$

where x' is a dummy integration variable. The right hand side of equation (21) is the difference of the flux at x and at $x=0$, obtained by directly integrating its divergence. After moving the second term in the right-hand side of equation (21) to the left-hand side, we assign the new left-hand side of equation (21) to the inner solution and the right-hand side of equation (21) to the outer solution. Thus,

$$\begin{aligned} & \frac{\partial}{\partial t} \int_0^\infty [\chi^{(F)}(\xi_f', t) - p(t)] d\xi_f' \\ & + \frac{1}{\delta} \frac{\partial}{\partial \xi_f} [(\chi^{(F)}(\xi_f = 0, t) + \psi^{(F)}(\xi_f = 0, t))] \\ &= \lim_{x \rightarrow 0} \frac{\partial}{\partial x} [\chi^{(B)}(x, t) + \psi^{(B)}(x, t)]. \end{aligned} \quad (22)$$

where ξ_f' is a dummy variable. The right-hand side of this expression is calculated from equations (8a) and (8b). Vice versa, the first term on the left-hand side is evaluated at the leading order by using equations (9a) and (10b) as

$$\begin{aligned} & \frac{\partial}{\partial t} \int_0^\infty [\chi^{(F)}(\xi_f', t) - p(t)] d\xi_f' \\ &= -\frac{\partial}{\partial t} \left[\int_0^\infty \frac{\partial^2 \psi^{(F)}(\xi_f', t)}{\partial^2 \xi_f'} d\xi_f' \right] \\ &= -\frac{\partial}{\partial t} \left[\frac{\partial}{\partial \xi_f} (\psi^{(F)}(\xi_f = \infty, t) - \psi^{(F)}(\xi_f = 0, t)) \right] \\ &= \frac{\partial}{\partial t} A_1^{(F)}(t). \end{aligned} \quad (23)$$

Then, to evaluate the second term on the left-hand side of equation (22), we apply the continuity of the ion flux at the polymer-CL interface as in equation (6b) by substituting $\xi_f = x/\delta$ and $\eta_l = x_{cl}/\sqrt{\delta}$ in the ion-blocking conditions. This yields

$$\begin{aligned} & \frac{1}{\delta} \frac{\partial}{\partial \xi_f} [(\chi(\xi_f = 0, t) + \psi(\xi_f = 0, t))] \\ &= -\mathcal{D}^* \phi \frac{\partial [\chi(\eta_l = 0, t) + \psi(\eta_l = 0, t)]}{\partial \eta_l}. \end{aligned} \quad (24)$$

The right-hand side of this expression is available from the solution of equation (13b). Summarizing these developments, the flux continuity condition in equation (22) can be conveniently expressed in the Laplace domain as

$$sA_1^{(F)}(s) + \phi \sqrt{s\mathcal{D}^*} C_3^{(L)}(s) = A_1^{(B)}(s). \quad (25)$$

We further enforce ion blocking condition at the polymer-electrode interface and ion flux continuity at the CL-electrode interfaces, by following the same procedure as above. This

results into two additional flux conditions expressed in the Laplace domain as

$$-sA_1^{(E)}(s) = A_1^{(B)}(s), \quad (26)$$

$$-C_3^{(G)}(s)\sqrt{s} = \sqrt{\delta\mathcal{D}^*}C_1^{(C)}(s). \quad (27)$$

Next, we enforce the continuity of electric displacement at the CL-polymer interface as required in equation (6c). Again, we revert to the time domain for derivations. First, the charge in the CL near the interface is evaluated by integrating equation (4a) as

$$\begin{aligned} -\varepsilon^* \left[\frac{\partial\psi_{cl}(x_{cl},t)}{\partial x_{cl}} - \frac{\partial\psi_{cl}(0,t)}{\partial x_{cl}} \right] \\ = \int_0^{x_{cl}} [\chi_{cl}(x'_{cl},t) - ap(t)] dx'_{cl}, \end{aligned} \quad (28)$$

where x'_{cl} is a dummy variable. Next, the second term on the left-hand side is moved to the right-hand side and the outer solution in equation (12b) and inner solutions at the top of the CL are used to evaluate the left- and right-hand sides, respectively. At the leading order, we have

$$\begin{aligned} -\varepsilon^* C_1^{(C)}(t) = \sqrt{\delta} \int_0^\infty [\chi^{(L)}(\eta'_l, t) - ap(t)] d\eta'_l \\ - \frac{\varepsilon^*}{\sqrt{\delta}} \frac{\partial\psi^{(L)}(\eta_l = 0, t)}{\partial\eta_l}. \end{aligned} \quad (29)$$

where η'_l is a dummy variable. By Laplace-transforming equation (29) and using for $\chi^{(L)}(\eta_l, s)$ in the first term on the right-hand side the solution of equation (13b), we obtain

$$\begin{aligned} -\varepsilon^* C_1^{(C)}(s) = \sqrt{\delta} \int_0^\infty C_3^{(L)}(s) e^{-\eta'_l \sqrt{s/\mathcal{D}^*}} d\eta'_l \\ - \frac{\varepsilon^*}{\sqrt{\delta}} \frac{\partial\psi^{(L)}(\eta_l = 0, s)}{\partial\eta_l}. \end{aligned} \quad (30)$$

Finally, by substituting in $\psi^{(L)}(\eta_l, s)$ the Laplace-transformed solution of equation (13a), and using the definition $\varepsilon^* = \varepsilon_{cl}\delta/(\varepsilon\phi)$, we find

$$-\varepsilon^* C_1^{(C)}(s) = \sqrt{\frac{\delta\mathcal{D}^*}{s}} C_3^{(L)}(s) + \frac{\sqrt{\delta}}{\phi} A_1^{(F)}(s). \quad (31)$$

To summarize, Equations (18a)–(20b), (25)–(27) and (31) constitute a linear system in the twelve unknown functions $A_0^{(B)}(s)$, $A_1^{(B)}(s)$, $A_1^{(F)}(s)$, $A_3^{(F)}(s)$, $A_1^{(E)}(s)$, $A_3^{(E)}(s)$, $C_0^{(C)}(s)$, $C_1^{(C)}(s)$, $C_0^{(L)}(s)$, $C_3^{(L)}(s)$, $C_0^{(G)}(s)$, $C_3^{(G)}(s)$. While the solution of the problem is, at this point, trivially tackled via computer aided algebra packages, the complete expressions for most of the coefficients and the resulting composite fields are too cumbersome to display. Fortunately, to understand the sensor behavior of the eIPMC under compression, only a subset of the solution data is necessary, as explained in the next section.

2.6. Equivalent circuit model for eIPMC compression sensor behavior

We characterize the eIPMC compression sensor behavior by extracting an equivalent circuit model from the solution of the governing equations. To this aim, we calculate the eIPMC electric current output (per unit nominal surface area). First, the non-dimensional charge storage at the electrodes (per unit nominal surface area) is calculated in the time domain from the jump of the electric displacement field at the interface, as calculated from the inner solution in region (E), see also [24, 28],

$$q(t) = - \left. \frac{\partial\psi^{(E)}(\xi_e, t)}{\partial\xi_e} \right|_{\xi_e=0} = -A_1^{(E)}(t). \quad (32)$$

Note that the charge scaling is consistent with the definition of [39]. Defining the non-dimensional current per unit area as the time rate of change of the stored charge, the current through the eIPMC in the Laplace domain is given by

$$\begin{aligned} I(s) = -sA_1^{(E)}(s) \\ = \frac{(ms\sqrt{s})\gamma p(s) + (ms\sqrt{s} + s^2)V(s)}{n(m\sqrt{s} + s) + 2s(m\sqrt{s} + 1) + m\sqrt{s} + 2s^2}, \end{aligned} \quad (33)$$

where we have introduced the following nondimensional parameters: transduction gain $\gamma = 1 - a = (1 - \phi)[1 - E_p/E_m] \approx 1 - \phi$, diffusivity parameter $m = \sqrt{\mathcal{D}^*\phi^2} = \sqrt{\mathcal{D}_{cl}\phi^2/(\delta\mathcal{D})}$, and permittivity parameter $n = d\phi/(h\varepsilon^*) = d\varepsilon/(h\delta\varepsilon_{cl})$.

This expression establishes the relationship between the current through the eIPMC, the voltage across its electrodes, and the external mechanical input. We denote now with $G(s)$ the coefficient multiplying $p(s)$ and with $Y(s)$ the coefficient multiplying $V(s)$. The current can thus be expressed as $I(s) = G(s)p(s) + Y(s)V(s)$. By solving for $V(s)$ and indicating with $Z(s) = 1/Y(s)$, we obtain

$$V(s) = Z(s)I(s) - Z(s)G(s)p(s), \quad (34)$$

which shows that the term $Z(s)$ represent a physical impedance (per unit area), and the mechanical input is equivalent to a voltage generator. To better understand the physical behavior of the eIPMC dynamic compression sensor, it is illustrative to isolate the expression of the impedance found above

$$\begin{aligned} Z(s) = \frac{2s^2 + (2m)s\sqrt{s} + (n+2)s + (n+1)m\sqrt{s}}{s^2 + ms\sqrt{s}} \\ = 2 + \frac{n+1}{s} + \frac{1}{s+m\sqrt{s}}. \end{aligned} \quad (35)$$

It is easy to show that this impedance can be realized via the series connection of a resistor, a capacitor, and the parallel connection of a capacitor and a Warburg impedance element [45], which models resistance to mass transfer. Thus, equations (34) and (35) describe the dynamics of the equivalent circuit displayed in figure 3, where the voltage generator $V_{\text{sense}} = Z(s)G(s)p(s)$ is controlled by the mechanical input and represents the mechanical to electrochemical

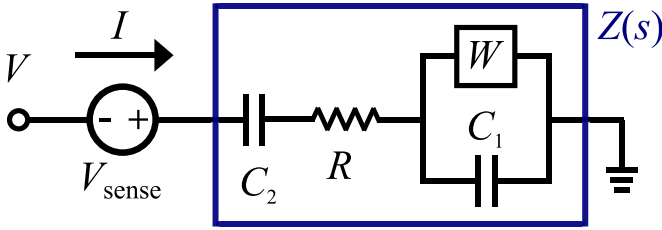


Figure 3. Equivalent circuit model of the eIPMC dynamic compression sensor. Note that the impedance of the Warburg element is $Z_W(s) = 1/(W\sqrt{s})$, see [40].

transduction. The impedance of the circuit in figure 3 is calculated as

$$\begin{aligned} Z(s) &= R + \frac{1}{C_2 s} + \frac{1}{C_1 s + W\sqrt{s}} \\ &= \frac{(C_1 C_2 R) s^2 + (C_2 R W) s\sqrt{s} + (C_1 + C_2) s + W\sqrt{s}}{(C_1 C_2) s^2 + (C_2 W) s\sqrt{s}}. \end{aligned} \quad (36)$$

By comparing the coefficients of the powers of s , the equivalent lumped circuit elements can be related to the parameters in equation (35). Specifically, because equation (35) is nondimensional, we find nondimensional values for the lumped circuit element as

$$C_1 = 1, \quad (37a)$$

$$C_2 = \frac{1}{1+n}, \quad (37b)$$

$$W = m, \quad (37c)$$

$$R = 2. \quad (37d)$$

Additionally, using equation (33), we can determine the expressions for nondimensional open circuit voltage V_{OC} or short circuit current I_{SC} by setting $I(s)$ or $V(s)$ equal to zero, respectively, in equation (34). These read

$$\begin{aligned} V_{OC} &= -V_{sense} \\ &= -Z(s) G(s) p(s) = -\frac{m\gamma p(s)}{m + \sqrt{s}}, \end{aligned} \quad (38a)$$

$$\begin{aligned} I_{SC} &= G(s) p(s) \\ &= \frac{(ms\sqrt{s})\gamma p(s)}{2s^2 + (2m)s\sqrt{s} + (n+2)s + (n+1)m\sqrt{s}}. \end{aligned} \quad (38b)$$

Figure 4 qualitatively depicts the nondimensional results of this modeling section. Panels (a) and (b) display the magnitude and phase of the eIPMC equivalent impedance of the circuit plotted using equation (35). Panels (c) and (d) display the magnitude and phase of the eIPMC OC voltage and SC current sensitivities plotted using equations (38a) and (38b). Finally, panels (e) and (f) display the OC voltage and SC current responses to a step input compression force, plotted using the inverse Laplace transform of equations (38a) and (38b) when $p(s) = p_0/s$. To illustrate the qualitative behavior of the system, in plotting these figures we have assumed $m = 1$ and

$n = 0.1$, which are consistent with our assumptions $\varepsilon^* = \mathcal{O}(1)$ and $\mathcal{D}^* = \mathcal{O}(1)$.

The effect of the parameters m and n on the eIPMC impedance can be understood from equation (35). The parameter m corresponds to the Warburg parameter W , related to the impedance of the Warburg element as $Z_W = 1/(W\sqrt{s})$. For vanishingly small values of m , the Warburg impedance becomes an open circuit. Thus, the equivalent circuit reduces to an RC circuit comprising the series connection of resistance R and a combined capacitance $C_1 C_2 / (C_1 + C_2)$. On the other hand, as m tends towards infinity, the Warburg impedance becomes a short-circuit, thus bypassing C_1 . In this case, the circuit reduces to an RC circuit comprising the series connection of resistance R and capacitance C_2 . On the other hand, the parameter n only controls the value of the capacitance C_2 . In particular, when $n \gg 1$, C_2 approaches an open circuit, while for $n \gg 1$, C_2 reduces to the nondimensional value 1. The impedance of our model has a typical low pass behavior dominated by C_2 , as seen in figure 4(a). For the particular present choice of parameters, a characteristic slope of -20dB/dec can be observed at low frequency, while at higher frequencies, the circuit effectively simplifies to a resistance R . The effects of the Warburg impedance can be seen in a narrow band in the neighborhood of $\omega/\omega_0 = 1$ for selected values of the m , and n parameter, manifesting themselves with a segment with slope close to -10dB/dec .

In figure 4(c), the OC voltage sensitivity displays a characteristic low pass behavior, maintaining an approximately constant value until reaching the cutoff frequency ω/ω_0 . As the frequency increases, the OC voltage sensitivity drops with a slope of -10dB/dec . In figure 4(d), the SC current sensitivity demonstrates a high pass behavior at low frequencies with a slope of 20dB/dec . Above the cutoff frequency, the SC current sensitivity displays a -10dB/dec slope as the frequency increases. For both voltage and current sensing, Warburg impedance-like effect seems to dominate the behavior above the cutoff frequency. This is a novel result which was not observed before in compression sensing of eIPMCs. Indeed, in our previous work, the modeling efforts were only able to identify the behavior below $\omega/\omega_0 \ll 1$.

To better understand the dynamic implications of our model, panels (e) and (f) depict the predicted time-domain response of the OC voltage and SC current of the eIPMC sensor to a step compressive force. These responses are obtained by numerically calculating the inverse Laplace transform of equations (38a) and (38b) where $p(s) = p_0/s$, that is, the transform of the unit step input. Observing both responses, it is apparent that over time, the response exhibits dynamics, with the SC current exhibiting a notably faster response compared to the OC voltage. Upon application of a step compression force, the OC voltage response gradually increases, eventually reaching its maximum value of 1 as $t \rightarrow \infty$. Initially, this increase is rapid (scaling as a diffusion-dominated \sqrt{t} time law) but its rate gradually slows down over time. Conversely, in the case of the SC current response, a peak value is rapidly achieved, followed by decay to its final value of 0 at $t \rightarrow \infty$. Note that the decay rate decreases over time, so neither response follows a traditional exponential behavior.

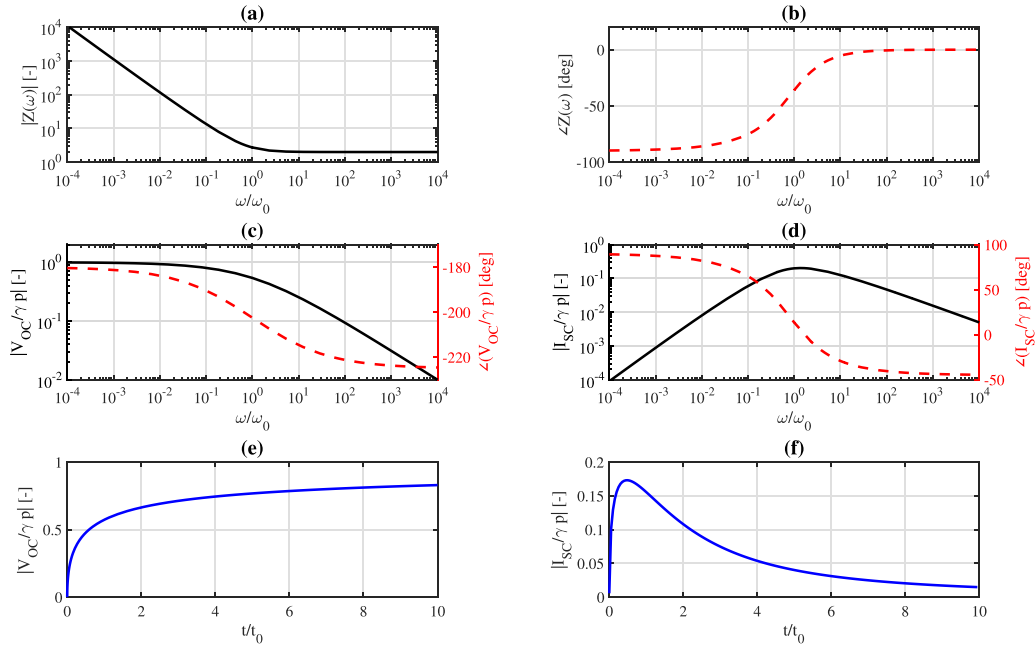


Figure 4. Nondimensional results of the modeling section: (a) Magnitude of the eIPMC equivalent impedance. (b) Phase of the eIPMC equivalent impedance. (c) Magnitude and phase of the eIPMC voltage sensitivity. (d) Magnitude and phase of the eIPMC current sensitivity. (e) Time domain OC voltage response to step input compression force. (f) Time domain SC current response of the eIPMC sample to step input compression force.

The predicted transient rising behavior of open circuit voltage and short circuit current in response to a constant input are in stark contradiction to the predictions of models ignoring the electrochemical effects of the CL, and will be investigated later with reference to experimental results.

In the modeling results of equations (38a) and (38b), the parameter γ is the transduction gain which depends on the effect of polymer-electrode interface topography on the mechanical properties of the eIPMC. This parameter can be understood as a tuning factor that lumps the degree of mechanical asymmetry between the top and bottom polymer-electrode interfaces. Particularly, $\gamma = 0$ for nominally identical flat interfaces and $\gamma > 0$ in the case of one-sided engineered interfaces, see also [28].

The physical interpretation of the circuit elements and equivalent circuit impedance, as well as the OC voltage and SC current behavior, will be discussed in the following section which also emphasizes the significant modeling predictions.

2.7. Discussion and predictions of the modeling framework

In this section, we aim at enhancing our understanding of the modeling results by providing their physical interpretation. Additionally, we will outline significant predictions derived from the modeling section to establish a foundation for our experimental studies. In particular, modeling results will highlight the predicted differences and trends expected between the properties and performance of traditional (control) IPMCs versus those of the proposed eIPMC compression sensors.

Our first step is to obtain the dimensional version of the circuit elements in equation (36). This can be done by

resorting to dimensional analysis of the definitions of current, voltage, and impedance. In particular, because $I = I_0 \tilde{I}$ with $I_0 = \varepsilon \mathcal{R} \mathcal{T} \mathcal{D} / (\mathcal{F} h \lambda_D^2)$, the characteristic impedance is $Z_0 = h \lambda_D^2 / (\varepsilon \mathcal{D})$, the characteristic capacitance is $C_0 = \varepsilon / \lambda_D$, and the characteristic Warburg parameter is $W_0 = \varepsilon \sqrt{\mathcal{D}} / (h \lambda_D^3)$. Therefore, we obtain for the dimensional values

$$C_1 = C_0 \tilde{C}_1 = \frac{\varepsilon}{\lambda_D}, \quad (39a)$$

$$C_2 = C_0 \tilde{C}_2 = \frac{C_0}{1+n} = \left((\varepsilon / \lambda_D)^{-1} + (\varepsilon_{cl} / d)^{-1} \right)^{-1}, \quad (39b)$$

$$W = W_0 \tilde{W} = W_0 m = \frac{\varepsilon \sqrt{\mathcal{D}_{cl} \phi^2}}{\lambda_D^2}, \quad (39c)$$

$$R = Z_0 \tilde{R} = \frac{2h \lambda_D^2}{\varepsilon \mathcal{D}}, \quad (39d)$$

where a superimposed tilde indicates nondimensional values.

Based on these dimensional values, the circuit model can be restructured as in figure 5, which illustrates a ‘physics-based’ circuit model of the eIPMC sensor, along with a schematic representation of the various electrochemical effects. The physics-based model includes three capacitances, function of the permittivity of the bulk and CL, the thickness of the CL, and the Debye screening length. The first capacitance C_1 in equation (39a), can be interpreted as the double-layer capacitance, developing over a characteristic thickness λ_D , near the CL-electrode interface, denoted as C_{DL} in the physics-based circuit. The capacitance C_2 in equation (39b), can be interpreted as two capacitances in series, C_{DL} and C_L . In this instance, C_{DL} represents the double-layer capacitance near the interface between the polymer and the movable electrode. On the other hand, C_L signifies the capacitance associated

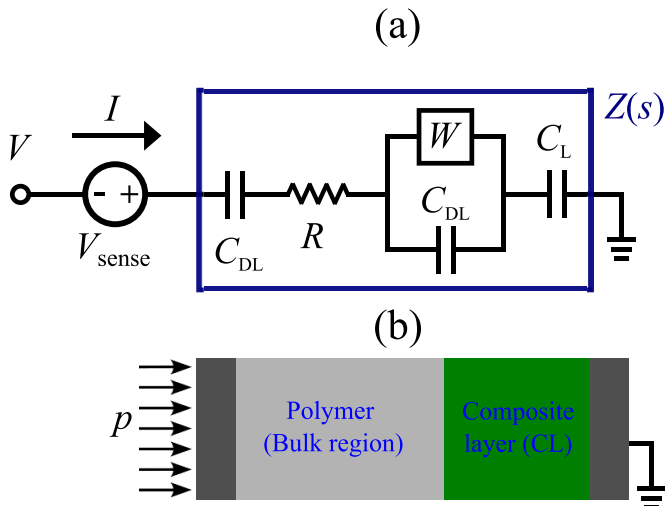


Figure 5. (a) Equivalent physics-based circuit model of the eIPMC dynamic compression sensor. (b) Schematic representation of the electrochemical effects.

to the charge storage in the CL, developing over a thickness d . Equation (39c) suggests that the Warburg impedance is influenced by counterion diffusion within the CL, the permittivity of the bulk region, and the Debye screening length. This impedance governs the diffusivity process and sensing behavior of the eIPMC. Finally, the circuit element R in equation (39d), represents the TTT resistance in the eIPMC sample.

Although our modeling framework is not immediately applicable to traditional IPMCs (with nominally flat electrodes and no engineered interfaces), the physics-based circuit model can however help inform predictions on the performance of eIPMCs versus conventional IPMCs when the latter are interpreted with the models of [40]. Specifically, in [40] the Warburg impedance model is used to account for electrode surface roughness. Thus, because $\varepsilon \ll \varepsilon_{cl}$ and $\mathcal{D} \gg \mathcal{D}_{cl}$, it follows that the parameter m is strongly dependent on the diffusivity of the CL and the polymer bulk region, while n hinges on their permittivity. In the idealized traditional IPMC sample, denoted in the following as ‘control’ sample, featuring two perfectly flat interfaces, the absence of an engineered CL results in a smaller value for parameter m and a larger value for parameter n compared to those of the eIPMC sample. Based on these observations, we summarize this section with the main theoretical predictions of our model ($P1 - P9$), to be verified later through specifically designed experiments.

P1: The OC voltage demonstrates a direct correlation with the asymmetry parameter γ , the diffusivity parameter m , and the externally applied pressure. This suggests that, for the same applied pressure, the eIPMC sample which is characterized by its asymmetric geometry and interfaces, exhibits higher OC voltage compared to the control sample. These findings are consistent with our earlier research [28, 39].

P2: The SC current demonstrates a direct correlation with the asymmetry parameter γ , the diffusivity parameter m , and the externally applied pressure and inverse correlation with the permittivity parameter n . This suggests that for the same applied pressure, the eIPMC sample which is characterized by its asymmetric geometry and interfaces, exhibits higher SC current compared to the control sample.

P3: Figures 4(e) and (f) indicate that the OC voltage has a much slower response, in terms of rise time, than the SC current to the step compressive load. The faster response of the SC current also makes this response more susceptible to noise. Noise sensitivity becomes more apparent when the noise has a similar or faster timescale compared to the system’s response time.

P4: Based on the qualitative predictions in figure 4 and on the circuit model, the OC voltage, SC current, and equivalent impedance of the circuit have similar cutoff frequencies. Using our assumptions for m and n , this is located at $\omega/\omega_0 \approx 1/(n+1)$.

P5: As the frequency of the external compression load increases beyond the cutoff frequency, the OC voltage and SC current sensitivity decrease. This suggests that the diffusion process lags behind the applied force, indicating an incomplete synchronization between the diffusion process and the applied force. Above the cutoff frequency, with an increase in frequency, the voltage and current sensitivities will reduce with a -10dB/dec slope, highlighting the role of diffusion-dominated behavior.

P6: The time domain OC voltage response of the eIPMC sensor to a step input compressive force of magnitude p_0 exhibits dynamics over time. This is in contrast to previous modeling efforts that neglected the effects of the CL and predicted instantaneous response to an input. The predicted dynamics in the response to a step input is consistent with what we have observed in our previous published studies [38, 39] and as such constitutes an important improvement in our modeling framework. Our model suggests that, as the input is applied, the voltage signal increases rapidly, scaling as \sqrt{t} , then its rate gradually slows down as time progresses. This behavior can be attributed to the diffusion process occurring within the eIPMC sample. From a physical perspective, when the step input force is initially applied, the diffusion process starts at its maximum rate, leading to the rapid increase in the OC voltage. However, as time progresses, the diffusion rate gradually decreases, resulting in a slower rate of increase in the OC voltage over time. The model predicts that the OC voltage settles to its final value $-\gamma p_0$ asymptotically (in infinite time).

P7: As shown in figure 4(e), the time domain step response of the eIPMC OC voltage, the transient starts synchronously to the applied input force, suggesting that the diffusion process within the eIPMC commences synchronously, without any

transmission delay, as soon as the step input force is applied. However, the voltage output does not track the compression step input, in contrast to what predicted by models neglecting the electrochemical effects of the CL.

P8: As shown in the time domain SC current response of the eIPMC sensor to a step input compressive force, a different behavior is observed compared to the OC voltage case. Upon the application of the unit step compression force, the SC current undergoes a rapid increase to reach its peak value, followed by a gradual decrease towards its final asymptotic value of 0. The rising response occurs over a much faster time scale than the decaying response. This observation is consistent with the notion of charge diffusion occurring within the eIPMC, and dominated by the properties of the CL.

P9: As depicted in figure 4(f), the time domain SC current response of the eIPMC starts immediately upon the application of the step input force, without any transmission delay. Note however that the peak value does not occur instantaneously at the time instant when the step input is applied, in contrast to what predicted by models neglecting the electrochemical effects of the CL.

To verify these predictions, experimental investigations will be conducted in the following sections. It is important to note that our modeling assumptions for an ideal control sample involve presuming completely smooth polymer-electrode interfaces on both the top and bottom surfaces. This would imply that the parameter γ is assumed to be zero for the control sample, resulting in zero OC voltage, SC current, and sensing voltage. However, experimental outcomes for the control sample are not expected to align precisely with these assumptions, as real interfaces are not perfectly smooth [37, 41]. The unavoidable asymmetry between the two electrodes in the control sample contributes to the small but non-zero values observed for OC voltage and SC current [28]. Electrode surface roughness is also to be expected in the eIPMC, but it is not explicitly modeled in this work. Therefore, when comparing model predictions of equivalent circuit elements, OC voltage, and SC current of the control and eIPMC samples with experimental findings, we will focus primarily on the qualitative assessment of our models and results.

In addition, due to the underlying hypothesis of linear sensing behavior, we will consistently focus on the discussion of voltage and current sensitivities in dynamic conditions. However, we remark that a comprehensive study on the behavior of eIPMCs under static, varying compression load conditions has been presented in our previous works [28, 38].

3. Fabrication and electrochemical testing

In this section, we report on the fabrication processes using the traditional IPMC fabrication method and the PAT for the control and eIPMC samples, respectively. To characterize the electrochemical behavior of the fabricated samples, electrochemical impedance spectroscopy (EIS) testing is employed to estimate the impedance of both plated control and eIPMC

samples. Based on the modeling section results, and our previous comprehensive process-structure-property relationship characterization presented in [39], the microstructure causing the asymmetry between two electrodes are expected to significantly affect the electrochemical properties of the eIPMC samples.

3.1. eIPMC fabrication

The eIPMC samples with engineered interface are fabricated using the PAT. This fabrication process is thoroughly illustrated in our previous work [38]. Here, for completeness, we provide only a brief description of the fabrication steps.

The process begins by abrasively roughening one side of the as-received Nafion-1110 membrane sheet using 400 grit sandpaper, creating two distinct sites for the development of metal-polymer interfaces and introducing deliberate asymmetry into the finalized eIPMC. This particular grit size is chosen based on its higher sensitivity under compression, as observed in our prior research [39]. After roughening, the samples undergo chemical cleaning with 3% hydrogen peroxide followed by rinsing in 1 M sulfuric acid to remove impurities. The cleaned Nafion is then plated using an electroless chemical reduction (ECR) procedure, involving stirring in a 0.02 M platinum solution and subsequent reduction with sodium borohydride. This primary plating is repeated three times to ensure sufficient platinum deposition. Secondary plating with aqueous tetraamineplatinum (II) chloridemonohydrate solution follows, also repeated three times to ensure the conductivity of the sample. The plated samples are then soaked in a 1 M lithium chloride solution to conclude the plating process. Notably, both control IPMC and eIPMC samples undergo identical plating processes in the same chemical batches to minimize variations inherent to the ECR process. Finally, the fabricated samples are cut to size for electrochemical testing and OC voltage and SC current measurements under dynamic compressive loads. When cutting the fabricated sensor, all edges are trimmed to prevent shorting within the sensor.

3.2. Electrochemical characterization

To verify our equivalent circuit modeling results and understand the impedance behavior of both control and eIPMC samples, EIS tests are performed on plated samples. Using this test, the impedance of the sample can be extracted over a broad range of frequencies. The setup is similar to what discussed in [28]. In this setup, a Gamry Interface 1000 potentiostat is used. The eIPMC and control samples, are cut to $1 \times 1 \text{ cm}^2$ dimensions. Adhesive copper tape is firmly attached to each surface electrode of the sample to connect it to the potentiostat. For the eIPMC sample, the surface with the abraded side was connected to the ground terminal of the Gamry potentiostat unit. All the electrochemical tests are performed 30 minutes after full submersion of the sample in deionized water. The excitation AC voltage is set to 10 mV rms, that is well below the thermal voltage which is approximately 25 mV. The frequency range between 0.01 Hz and 100 Hz with 20 points/decade. To ensure electroneutrality of each sensor,

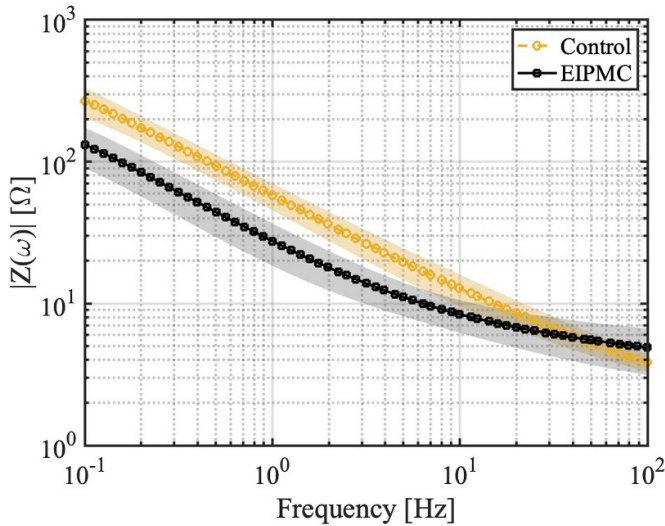


Figure 6. Impedance magnitude of the control and eIPMC samples from EIS measurements. Markers refer to mean values at each tested frequency, and shaded bands indicate one standard deviation.

an initial delay of 100s was used. Eight samples are used for this test, four eIPMC and four control samples. To ensure the repeatability, each sample is tested three times.

In figure 6, the impedance magnitude of both the eIPMC and control samples obtained from the EIS test is illustrated. Each impedance magnitude plot for the control and eIPMC samples represents the average of twelve measurements (with four samples, each measured three times). In this figure, markers refer to mean values at each frequency, and shaded bands showing one standard deviation, thus indicating the spread of experimental measurements. Overall, the graph indicates that for frequencies approximately below 20Hz, the eIPMC exhibits lower impedance as compared to the control sample. However, at frequencies exceeding 40Hz, the control samples generally display lower impedance than the eIPMC sample. As expected, especially in the low frequency range, the spread of experimental data is due to the effect of the engineered interfaces, and consistently with what observed in previous research, is larger for the eIPMC samples. Due to increased diffusion-dominated behavior, and thus somewhat slower time scales, eIPMC sensing is not expected to outperform control samples at very high frequencies. This effect can be anticipated by referring to a more pronounced low-pass behavior in the EIS data for the eIPMC samples.

To further validate our equivalent circuit model results, figure 7 displays EIS measurements, in terms of magnitude and phase, for one of the eIPMC samples, superimposed to a fitted circuit model as in equation (36) and in figure 3. These fits are plotted by assigning the circuit of figure 3 in the Gamry software as the electrochemical element equivalent circuit.

While experimental results for the magnitude are in excellent agreement with theoretical predictions, small discrepancies can be observed for the phase. At high frequencies, we hypothesize the unmodeled dynamics, likely a bulk capacitive behavior as observed in [41], may be contributing to added phase lag. Such effects are outside the frequency range of

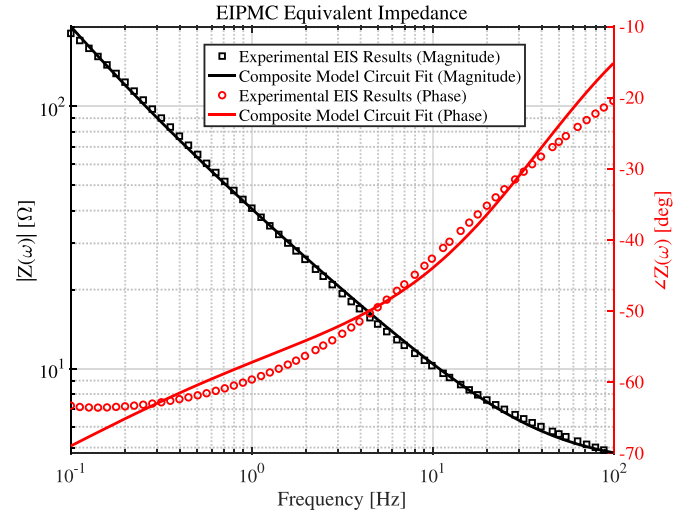


Figure 7. Representative impedance magnitude (black) and phase (red) measurements (markers) and fits (lines) for eIPMC experimental results using the equivalent circuit model in equation (36) and figure 3.

interest of this work. At low frequencies, we ascribe the discrepancies in part to the difficulties associated to low frequency spectroscopy (whereby one cycle extends for tens of seconds during which nonlinear effects may take place), in part to the small current magnitudes and difficulties associated in the discrimination of the phase, and in part, possibly, to numerical reasons in the system identification subroutines used. Despite these, we are confident that both magnitude and phase fits demonstrate that our proposed model can correctly capture the experimental data, thus supporting our modeling hypotheses and analytical work in section 2.

4. OC voltage and SC current sensing experiments

In this section, we aim to verify our modeling results and predictions from section 2 through experimental measurements of OC voltage and SC current sensing performance in dynamic conditions. These measurements are also crucial for establishing process-structure-property-performance relationships of the eIPMC sensor, which will be further explored in section 5. We begin by outlining the experimental setup, followed by an analysis of the samples responses to various dynamic compression sensing modes. These modes include the response to single sine, step, and chirp input compressive forces.

4.1. Experimental setup

Figures 8(a)–(c) depict the schematic of the experimental setup, as well as the side and the top view of the actual testbed, respectively. The setup utilizes a RIGOL DG1022 signal generator to generate desired electrical waveforms. These are amplified in a Vibration Research VR565 power amplifier to drive a Vibration Research VR5200 electrodynamic shaker that is used to impart the force input to the test article. To uniformly apply the compression force to the IPMC sample, two

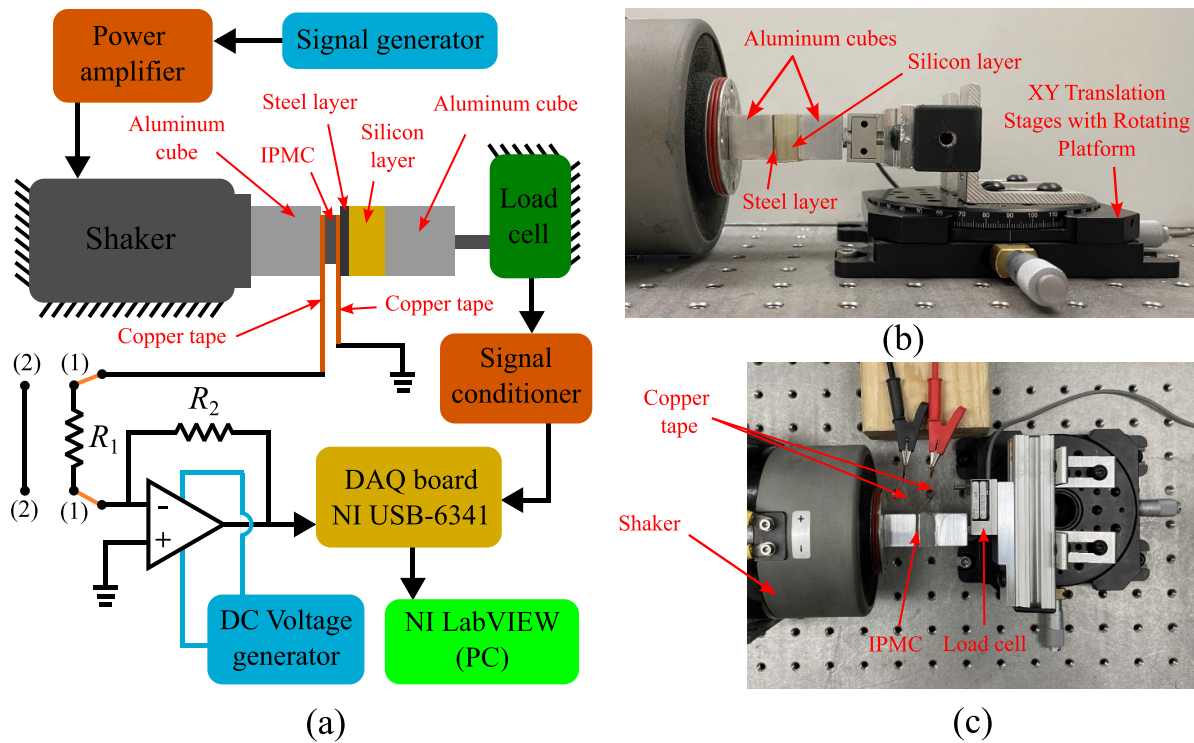


Figure 8. Experimental setup for eIPMC OC voltages and SC current measurements: (a) Schematic view, (b) Side view of the real setup without the eIPMC sample, (c) Top view of the real experimental setup with the eIPMC sample. Note that the circuits with (1)–(1) and (2)–(2) connections are being used for OC voltage and SC current measurements, respectively.

aluminum cubes with flat parallel surfaces are utilized. One cube is affixed to the shaker moving plate, while the other is securely attached to a load cell to measure the input forces to the sample. Both shaker and load cell are affixed to an optical table. A spring (collocated in series with the measurement chain), made from a thick flexible silicone layer, is interposed between the aluminum cubes to help align their surfaces under slight pre-compression force, ensuring a nearly uniform distribution of the compressive force on the IPMC surfaces. One side of this silicon layer, which contacts the IPMC sample, is covered with a thin steel plate to aid in distributing the compression force more uniformly. The IPMC sample is positioned between the cube fixed to the shaker tip and the steel layer covering the silicon layer. Both sides of the IPMC samples are covered with conductive copper tape, which connect the IPMC samples to the data acquisition circuit. Note that the inner side of the copper tape segments and the surfaces of the steel layer and aluminum cube in contact with the IPMC sample are insulated with non-conductive tape to prevent short circuits and intermittent contacts during the compression process.

In the experiments, in response to the provided mechanical actuation, two sets of signals are acquired, that is, the imparted force to the sensor and the IPMC electrical output, so as to construct useful input-output relationships. Specifically, to measure the applied force produced by the mechanical shaker a Transducer Techniques GSO-100 load cell (calibrated with known force) is used. The frame of the load cell is clamped to a $XY\theta$ stage used to fine-tune alignment and distance

between the two aluminum cubes and the pre-compression force applied to the eIPMC sample. The output voltage signal generated by the load cell, proportional to the applied force, is fed to a TMO-2 signal conditioner whose output is directed to a National Instruments data acquisition system NI USB-6341 DAQ board. Finally, the two conductive copper tape segments which cover the IPMC sample route the sensor output to an amplification circuit before acquisition. As shown in figure 8(a), the amplification circuit consists of an LM324N operational amplifier in inverting configuration, powered by a $\pm 5V$ DC power supply. When in configuration ‘(a)’, the circuit voltage output yields $V_{out} = (-R_2/R_1)V_{IPMC}$ for the OC voltage measurement. Similarly, when in configuration ‘(b)’, the circuit voltage output yields $V_{out} = -R_2I_{IPMC}$ for the SC current measurement. The circuit output voltage is fed to the same DAQ board. A NI LabVIEW custom virtual instrument (VI), configured with 10k samples to read and 1 kHz rate settings, is connected to the DAQ board for capturing data from IPMC and load cell sensors. This setup is used to apply external different compressive load to the eIPMC and control samples. For this purpose, in the next sections, the single sine, step, and chirp input force are used to measure the OC voltage and SC current performance of the eIPMC and control sensors.

4.2. Response to single sine input compressive force

To experimentally investigate the dynamic behavior of the eIPMC sensor, using the setup described above, we initially apply various sinusoidal pressure inputs to the sensor sample,

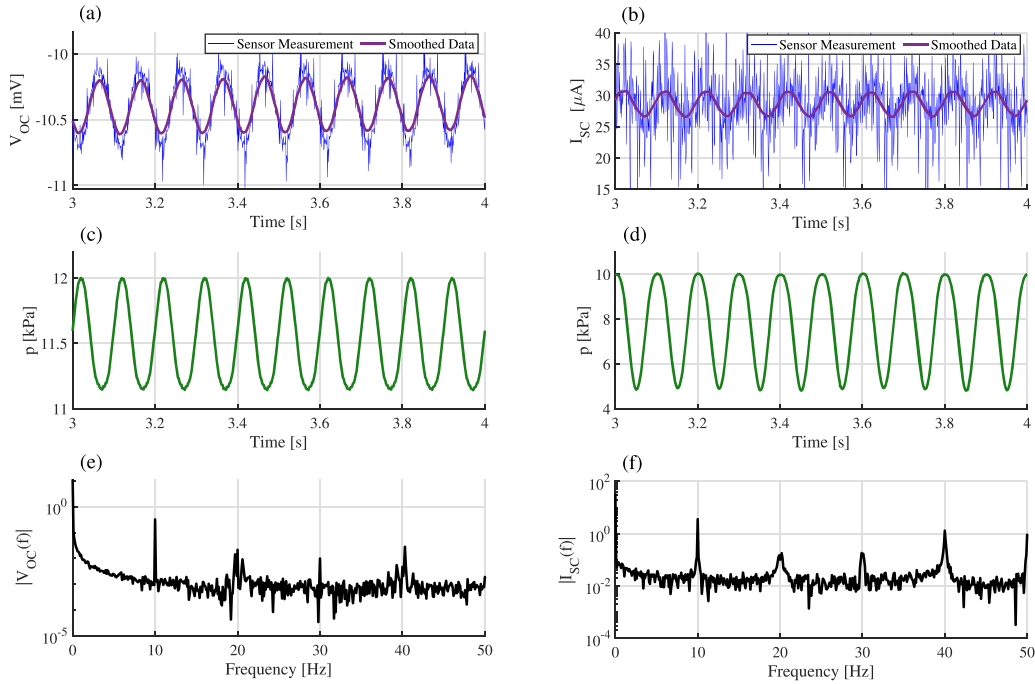


Figure 9. Sample OC voltage and SC current responses of the eIPMC sample to sinusoidal external pressure with 10Hz: (a) DAQ data (blue line) and smoothed data (purple line) of the OC voltage; (b) DAQ data (blue line) and smoothed data (purple line) of the SC current; (c) Applied periodic pressure using the shaker to extract the OC voltage; (d) Applied periodic pressure using the shaker to extract the SC current; (e) Single-sided Amplitude Spectrum of the DAQ data of OC voltage; and (f) Single-sided Amplitude Spectrum of the DAQ data of SC current.

with constant frequencies ranging from 1 Hz to 20 Hz. For these single sine measurements, we used $R_2 = 15.2 \text{ k}\Omega$ and $R_1 = 1.192 \text{ k}\Omega$ (nominal amplification gain of $R_2/R_1 = 12.75$) in the amplification circuit. For all other measurements, we utilized $R_2 = 23.62 \text{ k}\Omega$ and $R_1 = 1.192 \text{ k}\Omega$ (amplification gain of $R_2/R_1 = 19.81$). Figures 9(a) and (b) display the actual IPMC output (measured data divided by amplification gain) OC voltage and SC current data, along with their smoothed versions, for a representative input frequency of 10 Hz. The actual sensor measurements are obtained from dividing the measured DAQ data by the amplification gain, and attenuating six harmonics of the AC line power frequency (60 Hz) using single-notch filters. Figures 9(c) and (d) show the load cell data corresponding to the applied periodic pressure during the OC voltage and SC current measurements, respectively. It is evident that the OC voltage and SC current responses follow closely the applied pressure, albeit with possible phase shift, a result which aligns well with our predictions $P7$ and $P9$ in section 2.7.

To confirm the responsiveness of the sensor to a sinusoidal input, figures 9(e) and (f) show single-sided amplitude spectrum of the OC voltage and SC current raw data, respectively, which accurately reflect the applied frequency of 10 Hz. As predicted in the modeling section, because the response of the SC current is faster than the response of the OC voltage, its measurements are more susceptible to noise, especially when the noise has similar or faster nature than the SC current signal. This result is consistent with our prediction $P3$ in section 2.7.

The presence of higher harmonics (essentially, exact multiples of the forcing frequency) in the OC and SC response, may be in part ascribed to the possible nonlinearity of the eIPMC response, as well as to the non-ideal nature of the input signal. Indeed, while the applied pressure was intended to be perfectly sinusoidal, achieving perfect sinusoidal pressure experimentally, particularly at high frequencies, poses challenges. Several factors contribute to this deviation. Firstly, the stiffness and damping rate of the silicone spring may vary during compression and release cycles. Additionally, the silicone spring may exhibit non-linear, hysteretic, and/or viscoelastic behavior under certain conditions.

To compare the sensitivity to single sine input of eIPMC sensors against the performance of control samples over different frequencies for both OC voltage and SC current cases, the sensor responses were investigated over the band of input frequency between 1 and 20 Hz. Sensitivities of the samples at each integer-number frequency are calculated for both OC voltage and SC current data and plotted in figure 10. The results indicate that, in all frequency ranges, the eIPMC exhibits higher sensitivity than the control sample. Notably, in the low frequency OC voltage measurement range, sensitivity is improved of approximately 300%. Similarly, in the higher frequency SC current measurement range, sensitivity is improved of approximately 150%. These results are consistent with our modeling predictions $P1$ and $P2$ in section 2.7. Moreover, the difference between the sensitivity of the control and eIPMC samples increases with the frequency for SC current, whereas

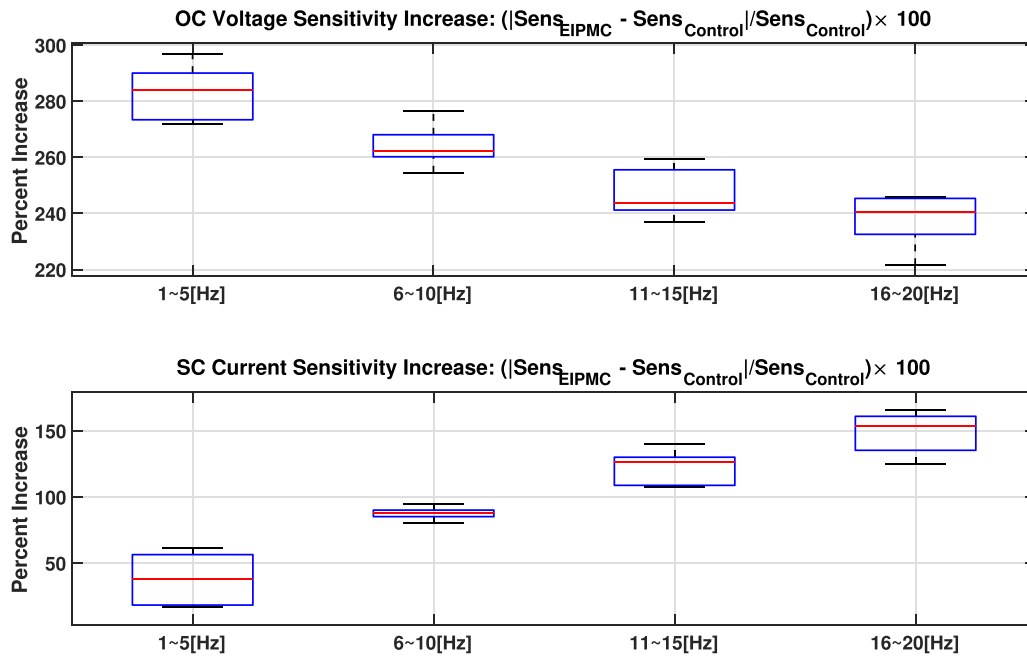


Figure 10. OC voltage and SC current sensitivity increase in eIPMC sample relative to the control sample in different frequency ranges.

the OC voltage shows the opposite trend, consistently with primary low-pass and high-pass behavior of the two sensing modes. This phenomenon can be explained in view of the different diffusion measurement mechanisms in OC voltage and SC current measurements.

4.3. Response to step input compressive force

Next, we investigate the OC voltage and SC current of an eIPMC sample in the time domain in response to a step compressive force. Our recent work [38] has investigated the OC voltage response of eIPMC under static compression step inputs with different amplitudes. The focus of this work is not on investigating the step responses under varying amplitude inputs, but rather on precisely examining the step response under a single amplitude compression input. Additionally, we have extended our measurements to SC currents. Representative measurements are shown in figures 11 and 12, respectively, for illustration. These voltage and current data are obtained from the raw measurements after applying a low-pass filter to attenuate frequencies above 55 Hz. For the OC voltage, the response is also detrended. It can be observed that both OC voltage and SC current results closely follow the jumps in the input step pressure in a synchronized manner, consistently with our predictions *P7* and *P9*, and qualitatively similar to the model predictions of the time domain responses in figures 4(e) and (f).

In particular, the experimental measurement of the OC voltage response indicates a behavior consistent with the predictions outlined in prediction *P6*, where upon the application of a step compressive force, the voltage starts increasing quickly at first, until plateauing at its maximum value at the end of the step period. While this transient is associated to the fast time scale of the highs and lows of the square wave input,

inspection of the long term behavior of the voltage response shows a moderate drift in the signal. This is to be ascribed to the presence of a mean value of the pressure input (pulsed from zero, rather than alternating between a positive and negative value). This mean value, akin to a ‘zero-th order’ Fourier series harmonic, contributes to a long term drift behavior of the voltage signal consistent with what predicted in figure 4(e) for an ideal step response.

Similarly, the experimental SC current depicted in figure 12 follows a pattern similar to prediction *P8*, with a rapid increase to the maximum value upon the application of the step compressive force, followed by a gradual decrease to reach the final value at the end of the step period. Because of the presence of very fast oscillations at the rising edge of the pressure signal, due to the mechanical nature of the force application, the current signal displays strong spikes in correspondence of the rising edge, as these high frequency components are amplified by the low pass nature of the current sensing mechanism. Interestingly, the current signal in figure 12 does not exhibit the drift in response to the mean value of the pressure wave due to the high-pass nature of current transduction. These observations align well with the anticipated trends, further validating the predictive capabilities of the model.

4.4. Response to chirp input compressive force

Finally, a linear sine sweep external pressure signal with 4 kPa amplitude (denoted as ‘chirp input’) ranging from 0.1 to 18 Hz is applied to both control and eIPMC samples over a time window of 30 seconds. Figure 13 illustrates the actual OC voltage and SC current measurements of both the control and eIPMC samples in response to the chirp input. Since the displayed signal represents the raw measurements (black lines), without applying any filter, its smoothed version (purple lines) is also

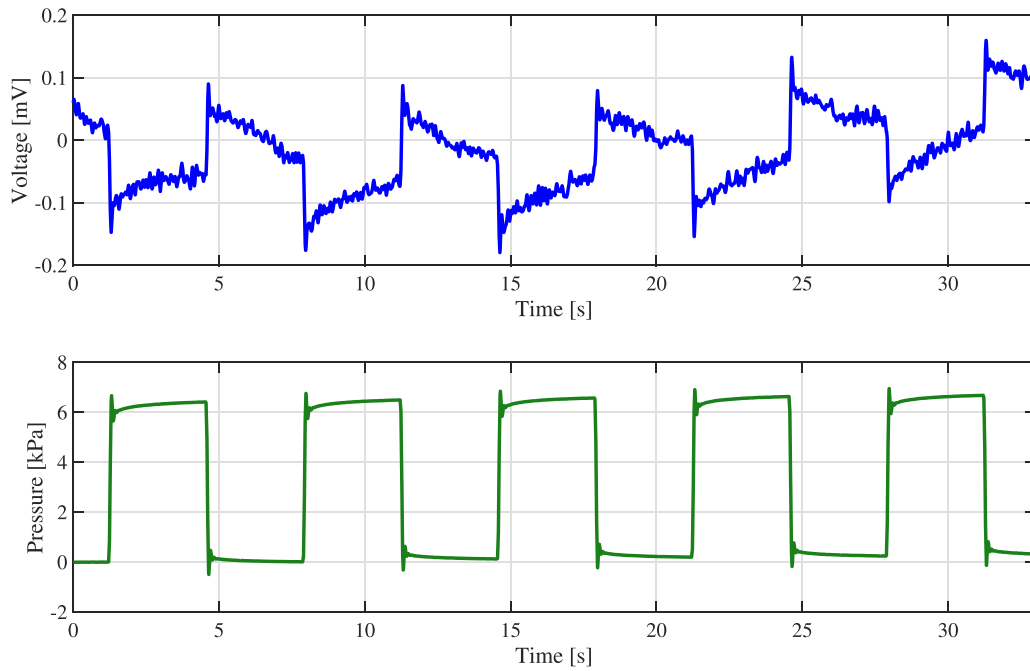


Figure 11. OC voltage response (top plot) of the eIPMC sample to step compression pressure (bottom plot).

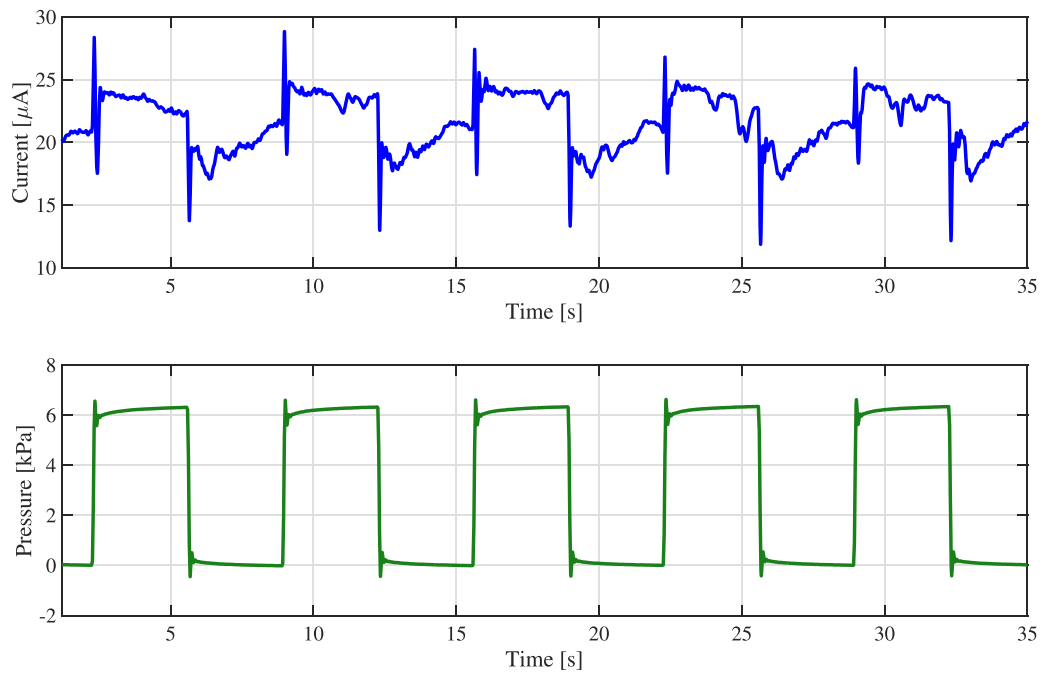


Figure 12. SC current response (top plot) of the eIPMC sample to step compression pressure (bottom plot).

included in the plots, to help observation and analysis. The main feature of the OC voltage and SC current of the eIPMC sample is that they exhibit a -10 dB/dec slope, consistent with the prediction from the modeling results shown in figures 4(c) and (d) and our prediction $P5$ in section 2.7. Conversely, no clear scaling dynamic trend is evident in the results from the output of the control sample.

In figure 13, the chirp OC voltage and SC current responses may not provide a very reliable estimate of the response

at very low frequencies, due to the relatively short duration of the excitation window. As a result, determining the exact cutoff frequency is challenging. However, over the band between 1 to 18 Hz, the experimental data exhibit a slope that corresponds to the modeling predictions. In addition, we remark that unmodeled effects, including the drift and time-dependent behavior of the eIPMC samples, complicate the precise quantitative comparison between the modeling and experimental results. Nevertheless, the qualitative trends are

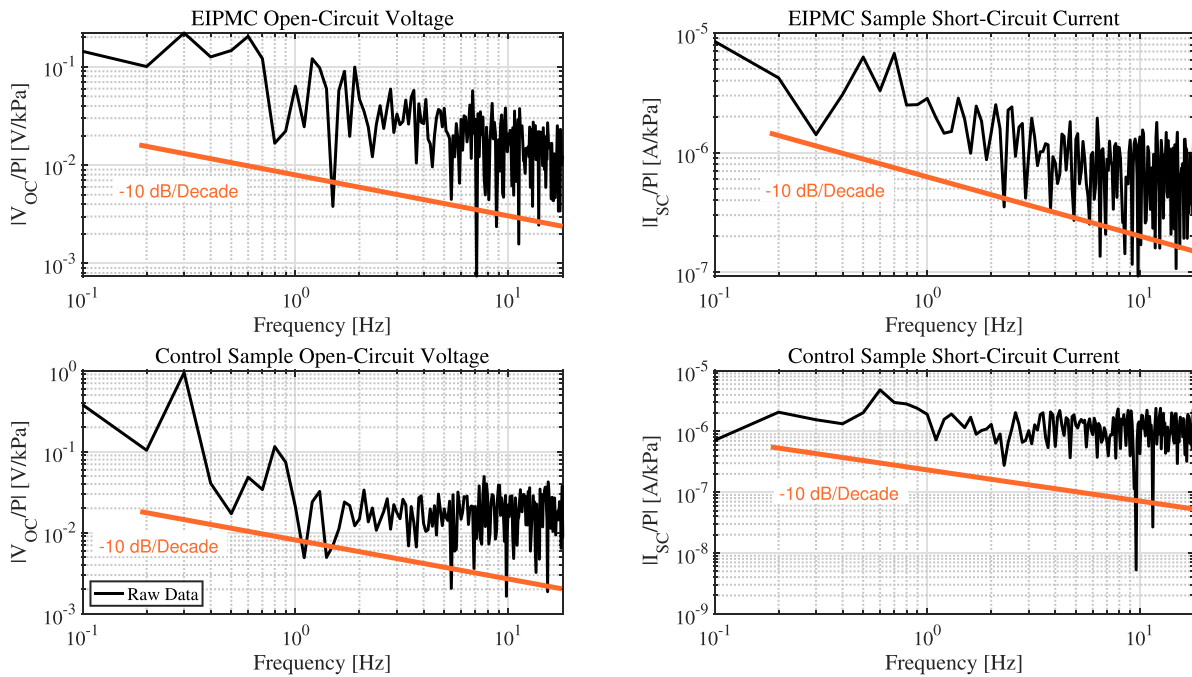


Figure 13. OC voltage and SC current sensitivities of control and eIPMC samples under chirp compressive force. Black lines refer to raw spectral data, and the orange line is meant as a visual reference for the -10 dB/dec slope.

correctly captured, thus essentially validating our modeling approach and results.

5. Discussion

The results and predictions derived from our modeling provide a comprehensive understanding of eIPMC sensor behavior, enabling a more robust correlation among the process-structure-property-performance relationships. While the process-structure-property connection in eIPMCs was extensively investigated in our previous works [28, 39], characterization of the performance in dynamic sensing condition was incomplete. In this work, the OC voltage and SC current predictions of our modeling framework were presented and verified via designed experimental campaigns. Experiments included the dynamic voltage and current response to single sine, step input, and chirp excitations. To the best of our knowledge, this is the first time that these dynamic characterizations are presented for eIPMC systems. Comparison of experimental findings for traditional IPMCs and novel eIPMCs are found to be consistent with our modeling results and demonstrate superior performance of our sensors as compared to the control samples.

In light of the presented analytical and experimental results, the following observations are in order. As described in section 3.1, eIPMC sensors were fabricated through PAT with one side abraded surfaces (microfeatures). The microstructure resulting from PAT was investigated in our previous work [39] via SEM imaging, to provide surface characterization of

both eIPMCs and conventional IPMCs before and after the plating process. SEM images showed the distinctive pattern of abraded surfaces and grooves generated by the PAT. In this work, we incorporated the mechanical and electrochemical properties of this region by modeling a separate CL layer. The engineered interface has two effects on eIPMC sensor behavior. First, it augments the surface area of the polymer-electrode interface, thereby increasing the capability for charge accumulation near the electrode, thus enhancing the sensor's overall capacitive behavior. Second, because of enhanced metal protrusions within the polymer, it amplifies the inhomogeneous strain distribution and modifies the charge dynamics within the polymer. Both these factors, consequently, improve mechanical and electrochemical properties of the sensor and can synergistically improve its performance.

The effect of electrochemical asymmetry of the CL is captured in the modeling framework in two ways. Of the three lumped capacitances identified by the circuit model, two are identical double-layer capacitances formed at the polymer-electrode and polymer-CL interfaces, independent of CL properties, see equation (39a). Vice versa, the third capacitor describes the capacitance due to the CL, see equation (39b). Interestingly, if the CL is assimilated to a flat plate capacitor, the characteristic separation d of the plates coincides with the CL thickness, hinting to absence of charge boundary layers in the CL region. The CL is also responsible for a Warburg impedance effect, see equation (39c). This resistance to ion migration models diffusion processes occurring within the polymer membrane. The Warburg impedance effect arises from the electrochemical properties of the CL and was not

explicitly incorporated in our previous work [39]. However, it provides important insights into the transport properties of IPMC materials, and is the key to explaining the sensing step response and its associated time dynamics, ultimately influencing OC voltage, SC current, and overall sensor behavior. As compared to traditional IPMCs, for which CLs can be expected to occur due to the morphology unpredictably created by the ECR fabrication method [40], in our novel eIPMCs large scale CLs are deliberately introduced via the engineered electrode, leading to superior sensing behavior compared to the control sample. These conclusions are supported by the EIS results presented in section 3.2 which show that the eIPMC sample exhibits smaller impedance at low frequency, compared to the control sample. This important experimental result suggests enhanced diffusion and ion transfer within the polymer membrane of the eIPMC sample due to the presence of the engineered CL.

While the proposed model displays predictive capabilities and experimentally validated qualitative results, it is important to acknowledge some limitations. In particular, our model assumes perfectly flat interfaces at the polymer-electrodes for IPMCs and eIPMCs, and at the CL-electrode and CL-polymer for eIPMCs. For IPMCs, this hypothesis would result in no mechanical asymmetry and homogeneous strain distribution. However, actual IPMCs exhibit roughness at both interfaces [37], creating mechanical asymmetry, and likely two CL capacitance and two Warburg impedance effects. This roughness contributes to the control sample's sensing behavior, observed in the experiments. Consistently with our developments, the sensitivity of traditional IPMCs is however much less than that of eIPMCs, which outperform their traditional counterparts in both voltage and current sensing tests, at low and high frequencies. A second effect observed in practice, but not explicitly accounted for in the model (stemming from the neglected surface roughness), lies in the development of large surface areas. Surface characterization results in [39] revealed mud-crack-like islands on the electrode surface, with a notably higher abundance observed in eIPMC samples. This increased presence of islands suggests a larger actual surface area development, indicating a more pronounced capacitive behavior for eIPMCs. This is reflected in the low frequency EIS results which indirectly support this observation. Overall, these effects impact the electrochemical behavior of the sensor, effectively enhancing its sensing capabilities.

Finally, the experimental performance results of eIPMC sample, including OC voltage and SC current dynamic sensing, were analyzed in detail. These results offer valuable insights into the sensor's behavior under compressive loads. As predicted by our modeling, the eIPMC sample are endowed by larger CL capacitance and Warburg impedance compared to the control sample, enhancing its dynamic sensing capabilities. Our compression sensors demonstrate optimal performance within a specific frequency range. Above the cutoff frequency, the sensitivity of the sensor decreases as the frequency increases, with typical slope of -10 dB/dec. This phenomenon reflects the diffusion mechanism within the eIPMC

sensors, where the diffusion process is too slow to track the applied force at higher frequencies.

6. Conclusions

This paper investigates the dynamical behavior of eIPMC sensors under compressive external loads, both analytically and experimentally. A detailed model incorporating a CL for the abraded interface between the polymer and electrode was developed to explicitly include the effect of mechanical and electrochemical asymmetries. Additionally, a new equivalent circuit model for eIPMCs with one engineered electrode was introduced. The model provides useful insight to better understand the superior sensing mechanism of eIPMCs under dynamic compression. The modeling results and predictions, presented at the end of modeling section, serves as the basis for our experimental investigations. To investigate the mechano-chemo-electrical behavior of the IPMC and eIPMC samples experimentally, these were fabricated using both traditional fabrication methods and a PAT. To further study the electrochemical behavior, EIS tests are performed on the samples. Finally, the experimental performance of eIPMCs in terms of OC voltage and SC current dynamic sensing, are analyzed in detail. Experimental findings on EIS test, OC voltage, and SC current align well with the qualitative modeling predictions, providing robust validation and advancing our understanding of eIPMC sensor behavior. As predicted by our modeling, the eIPMC sample are endowed by larger CL capacitance and Warburg impedance compared to the control sample, enhancing its dynamic sensing capabilities. The sensitivity comparison between the IPMC and eIPMC samples at single frequencies ranging from 1 to 18, Hz shows an increase of 220 to 290% in open-circuit voltage and 17 to 166% in SC current sensitivities. This confirms the improved sensitivity of eIPMCs under dynamic loads compared to traditional IPMCs over a broad actuation frequency range. These findings suggest that eIPMC sensors are well-suited to be utilized under dynamical compressive loads, potentially expanding their applications in various critical engineering scenarios. Future work will focus on the exploration of different sensing modes enabled by eIPMCs.

Data availability statement

The data cannot be made publicly available upon publication because no suitable repository exists for hosting data in this field of study. The data that support the findings of this study are available upon reasonable request from the authors.

Acknowledgments

This research was supported, in part, by the National Science Foundation under Grants No. 1809852, 1809455, 1847513 and

1545857. Any opinions, findings, and conclusions or recommendations expressed in this material are those of the authors and do not necessarily reflect the views of the sponsor.

ORCID iDs

Omid Fakharian  <https://orcid.org/0000-0003-0449-4696>

William S Nagel  <https://orcid.org/0000-0002-9215-4562>

Kam K Leang  <https://orcid.org/0000-0003-1189-1673>

Matteo Aureli  <https://orcid.org/0000-0003-4242-0081>

References

- [1] Hao Y, Zhang S, Fang B, Sun F, Liu H and Li H 2022 A review of smart materials for the boost of soft actuators, soft sensors and robotics applications *Chin. J. Mech. Eng.* **35** 37
- [2] Pérez P A L, Lopez R A and Femat R 2020 *Control in Bioprocessing: Modeling, Estimation and the use of Soft Sensors* (Wiley)
- [3] Patel S, Park H, Bonato P, Chan L and Rodgers M 2012 A review of wearable sensors and systems with application in rehabilitation *J. Neuroeng. Rehab.* **9** 21
- [4] Amjadi M, Kyung K-U, Park I and Sitti M 2016 Stretchable, skin-mountable and wearable strain sensors and their potential applications: a review *Adv. Funct. Mater.* **26** 1678–98
- [5] Park J, Lee Y, Cho S, Choe A, Yeom J, Ro Y G, Kim J, Kang D-h, Lee S and Ko H 2024 Soft sensors and actuators for wearable human–machine interfaces *Chem. Rev.* **124** 1464–534
- [6] Duan S, Zhao F, Yang H, Hong J, Shi Q, Lei W and Wu J 2023 A pathway into metaverse: Gesture recognition enabled by wearable resistive sensors *Adv. Sens. Res.* **2** 2200054
- [7] Zhao B, Dong Z and Cong H 2022 A wearable and fully-textile capacitive sensor based on flat-knitted spacing fabric for human motions detection *Sensors Actuators A* **340** 113558
- [8] Yuan Y, Chen H, Xu H, Jin Y, Chen G, Zheng W, Wang W, Wang Y and Gao L 2022 Highly sensitive and wearable bionic piezoelectric sensor for human respiratory monitoring *Sens. Actuators A* **345** 113818
- [9] Chen M, He Y, Liang H, Zhou H, Wang X, Heng X, Zhang Z, Gan J and Yang Z 2022 Stretchable and strain-decoupled fluorescent optical fiber sensor for body temperature and movement monitoring *ACS Photonics* **9** 1415–24
- [10] Shahinpoor M 2015 *Ionic Polymer Metal Composites (IPMCs): Smart Multi-Functional Materials and Artificial Muscles* (Royal Society of Chemistry)
- [11] Wang H, Yang L, Yang Y, Zhang D and Tian A 2023 Highly flexible, large-deformation ionic polymer metal composites for artificial muscles: Fabrication, properties, applications and prospects *Chem. Eng. J.* **469** 143976
- [12] MohdIsa W, Hunt A and HosseinNia S H 2019 Sensing and self-sensing actuation methods for ionic polymer-metal composite (IPMC): a review *Sensors* **19** 3967
- [13] Shahinpoor M and Kim K J 2005 Ionic polymer-metal composites: IV. Industrial and medical applications *Smart Mater. Struct.* **14** 197–214
- [14] Wang G, Sun Y, Ji A, Yin G, Ge H, Liu X, Tong X and Yu M 2024 Review on the research progress and application of IPMC sensors *J. Bionic Eng.* **21** 1–30
- [15] Zhao C, Wang Y, Tang G, Ru J, Zhu Z, Li B, Guo C, Li L and Zhu D 2022 Ionic flexible sensors: mechanisms, materials, structures and applications *Adv. Funct. Mater.* **32** 2110417
- [16] Porfiri M 2019 Sensing mechanical deformation via ionic polymer metal composites: a primer *IEEE Instrum. Meas. Mag.* **22** 5–12
- [17] Aureli M and Porfiri M 2013 Nonlinear sensing of ionic polymer metal composites *Contin. Mech. Thermodyn.* **25** 273–310
- [18] Gudarzi M, Smolinski P and Wang Q-M 2017 Bending mode ionic polymer-metal composite (IPMC) pressure sensors *Measurement* **103** 250–7
- [19] Farinholt K and Leo D J 2004 Modeling of electromechanical charge sensing in ionic polymer transducers *Mech. Mater.* **36** 421–33
- [20] Biddiss E and Chau T 2006 Electroactive polymeric sensors in hand prostheses: Bending response of an ionic polymer metal composite *Med. Eng. Phys.* **28** 568–78
- [21] Pugal D, Jung K, Aabloo A and Kim K J 2010 Ionic polymer-metal composite mechano-electrical transduction: review and perspectives *Polymer Int.* **59** 279–89
- [22] Bahramzadeh Y and Shahinpoor M 2011 Dynamic curvature sensing employing ionic-polymer-metal composite sensors *Smart Mater. Struct.* **20** 094011
- [23] Farinholt K M, Pedrazas N A, Schluneker D M, Burt D W and Farrar C R 2009 An energy harvesting comparison of piezoelectric and ionically conductive polymers *J. Intell. Mater. Syst. Struct.* **20** 633–42
- [24] Aureli M, Prince C, Porfiri M and Peterson S D 2010 Energy harvesting from base excitation of ionic polymer metal composites in fluid environments *Smart Mater. Struct.* **19** 015003
- [25] Giacomello A and Porfiri M 2011 Underwater energy harvesting from a heavy flag hosting ionic polymer metal composites *J. Appl. Phys.* **109** 084903
- [26] Cha Y, Verotti M, Walcott H, Peterson S D and Porfiri M 2013 Energy harvesting from the tail beating of a carangiform swimmer using ionic polymer metal composites *Bioinsp.* **8** 036003
- [27] Cha Y, Shen L and Porfiri M 2013 Energy harvesting from underwater torsional vibrations of a patterned ionic polymer metal composite *Smart Mater. Struct.* **22** 055027
- [28] Histed R, Ngo J, Hussain O A, Lapins C K, Fakharian O, Leang K K, Liao Y and Aureli M 2021 Ionic polymer metal composite compression sensors with 3D-structured interfaces *Smart Mater. Struct.* **30** 125027
- [29] Gudarzi M, Smolinski P and Wang Q-M 2017 Compression and shear mode ionic polymer-metal composite (IPMC) pressure sensors *Sensors Actuators A* **260** 99–111
- [30] Volpini V, Bardella L, Rodella A, Cha Y and Porfiri M 2017 Modelling compression sensing in ionic polymer metal composites *Smart Mater. Struct.* **26** 035030
- [31] Volpini V, Bardella L, Rodella A, Cha Y and Porfiri M 2017 A Theoretical Framework for the Study of Compression Sensing in Ionic Polymer Metal Composites *Electroactive Polymer Actuators and Devices (Eapad) 2017* vol 10163 (SPIE) pp 90–95
- [32] Volpini V and Bardella L 2021 Asymptotic analysis of compression sensing in ionic polymer metal composites: The role of interphase regions with variable properties *Math. Eng.* **3** 1–31
- [33] Tang G, Zhao X, Ji Y, Zhao C, Mei D and Wang Y 2023 Influence of contact characteristics on pressure sensing of IPMC sensors *Intelligent Robotics and Applications* (Springer) pp 119–27
- [34] Wang Y, Tang G, Zhao C, Mei D, Zhao X, Ji Y and Li B 2022 The effects of contact area on pressure sensing of ionic polymer metal composite sensor with a soft substrate *Smart Mater. Struct.* **31** 065013
- [35] Zangrilli U and Weiland L M 2011 Prediction of the ionic polymer transducer sensing of shear loading *Smart Mater. Struct.* **20** 094013
- [36] Kocer B, Zangrilli U, Akle B and Weiland L 2015 Experimental and theoretical investigation of ionic polymer

- transducers in shear sensing *J. Intell. Mater. Syst. Struct.* **15** 2042–54
- [37] Aureli M, Lin W and Porfiri M 2009 On the capacitance-boost of ionic polymer metal composites due to electroless plating: theory and experiments *J. Appl. Phys.* **105** 104911
- [38] Nagel W S, Hussain O A, Fakharian O, Aureli M and Leang K K 2022 Surface roughness effects on ionic polymer-metal composite (IPMC) sensitivity for compression loads *Electroactive Polymer Actuators and Devices (EAPAD) XXIV* (<https://doi.org/10.1117/12.2613127>)
- [39] Nagel W S, Fakharian O, Aureli M and Leang K K 2024 Engineered IPMC sensors: modeling, characterization and application towards wearable postural-tactile measurement *Smart Mater. Struct.* **33** 015035
- [40] Cha Y, Aureli M and Porfiri M 2012 A physics-based model of the electrical impedance of ionic polymer metal composites *J. Appl. Phys.* **111** 124901
- [41] Aureli M and Porfiri M 2012 Effect of electrode surface roughness on the electrical impedance of ionic polymer-metal composites *Smart Mater. Struct.* **21** 105030
- [42] Cha Y and Porfiri M 2014 Mechanics and electrochemistry of ionic polymer metal composites *J. Mech. Phys. Solids* **71** 156–78
- [43] Porfiri M 2008 Charge dynamics in ionic polymer metal composites *J. Appl. Phys.* **104** 104915
- [44] Nayfeh A H 1981 *Introduction to Perturbation Techniques* (Wiley-Interscience)
- [45] Bard A J and Faulkner L R 2001 *Electrochemical Methods: Fundamentals and Applications* (Wiley)